Cell Biol Toxicol (2025) 41:85
https://doi.org/10.1007/s10565-025-10024-8

RESEARCH

IGFBP3 enhances adipose-derived stem cell function in soft tissue injury repair via ITGB1 and ERK pathway activation

Sirui Tian · Haiyang Yu · Ruoxuan Yang · Heshi Wang · Baohong Zhao · Danning Wang

Received: 8 July 2024 / Accepted: 13 April 2025

Abstract Soft tissue injury (STI) is a prevalent condition that requires effective therapeutic approaches. The focus of this investigation was to elucidate the molecular mechanisms linked to the IGFBP3 protein in adipose-derived stem cells (ADSCs) for STI repair, utilizing single-cell multiomics technology and a 3D bioprinting model. Establishment of a mouse-based STI model facilitated the comparison of cellular compositions and communication variances between wounded and normal tissues through single-cell RNA sequencing (scRNA-seq). High-throughput transcriptomics and bioinformatics analysis pinpointed IGFBP3 as a key target in ADSCs related to STI repair. In vitro experiments assessed IGFBP3's effects on ADSCs' epithelial cell differentiation, proliferation, and migration using various assays and lentivirus transfection to manipulate IGFBP3 expression. A 3D bioprinting technique was used to create an ADSCs-IGFBP3 peptide self-assembling hydrogel scaffold, characterized by Fourier-transform infrared spectroscopy, X-ray diffraction, SEM, and TEM. The scaffold's efficacy was validated in an animal model. Results showed nine cell subtypes in both normal and injured tissues, with increased ADSCs in STI tissues exhibiting enhanced connectivity and interactions. RNA-seq analysis confirmed IGFBP3 as crucial for ADSCs and STI. In vitro and 3D bioprinting experiments, along with animal model validation, confirmed IGFBP3's role in STI repair. Upregulation of IGFBP3 in ADSCs promoted epithelial cell differentiation by enhancing ITGB1 expression, activating the ERK pathway to boost cell proliferation and migration. This study highlights IGFBP3's significant role in ADSCs for STI repair, providing potential molecular targets for developing new treatments. The findings offer valuable insights into IGFBP3's mechanisms, aiding in advancing STI therapeutic strategies.

Highlights

- This research presents the initial discovery of the crucial role of IGFBP3 protein in ADSCs in the repair of STIs.
- Through single-cell multiomics technology and a 3D bioprinting model, this study found that high expression of IGFBP3 in ADSCs can promote epithelial cell differentiation.

Supplementary Information The online version contains supplementary material available at https://doi.org/10.1007/s10565-025-10024-8.

S. Tian · R. Yang · H. Wang · B. Zhao · D. Wang (✉)
Department of Oral Implantology, School and Hospital of Stomatology, Liaoning Provincial Key Laboratory of Oral Diseases, China Medical University, No. 117 Nanjing North Street, Heping District, Shenyang 110002, Liaoning Province, China
e-mail: dnwang@cmu.edu.cn

H. Yu
Comprehensive Emergency Department, Shenyang Stomatological Hospital, Shenyang 110002, Liaoning, China

- Bioinformatic analysis indicates that in STI, there is a closer interaction and enhanced mutual influence between ADSCs and other cells.
- Experimental validation in vitro and in animal models provides additional evidence supporting the crucial function of IGFBP3 in STI recovery.
- The research introduces original molecular targets and an intellectual underpinning to tackle STI, with significant potential for clinical applications.

Keywords Soft tissue injury · Adipose-derived stem cells · IGFBP3 protein · Single-cell multiomics · 3D bioprinting · Epithelial cell differentiation

Introduction

Soft tissue injury (STI) is a prevalent clinical issue, and its treatment and repair have long been significant research topics in the medical field (Thornhill et al. 2022; Nabil et al. 2022; Nie and Zhang 2022). In the process of repairing STI, cellular factors and signaling pathways play vital roles, among which adipose-derived stem cells (ADSCs) have garnered considerable attention as a potential therapeutic source (Liu et al. 2024). According to the literature, ADSCs are a type of multipotent stem cell that can be relatively easily obtained from adipose tissue. They possess autonomous renewal capacity and the potential to differentiate into a variety of tissue-specific cell types, including but not limited to hepatocytes, neurons, endothelial cells, renal epithelial cells, and epithelial cells (Al-Ghadban and Bunnell 2020; Khazaei et al. 2021). These characteristics position ADSCs as a significant resource in regenerative medicine and tissue engineering. Moreover, the differentiation potential of ADSCs extends to generating epithelial cells, facilitating the process of skin wound healing. With their pluripotency, promotion of angiogenesis, anti-inflammatory properties, and wound-healing capabilities, ADSCs offer new therapeutic strategies for STI treatment, indicating promising applications (Mazini et al. 2020; Schneider et al. 2023; Tang et al. 2022).

In ADSCs cells, IGFBP3 (Insulin-like growth factor binding protein 3) garners significant attention in research, yet its mechanism of action in repairing STI remains incompletely understood (Teufelsbauer et al. 2019; Wang et al. 2019). By employing bioinformatics analysis combined with transcriptomic techniques, researchers can comprehensively comprehend the expression characteristics of IGFBP3 in ADSCs cells and its potential roles in the repair of STI (Xiang et al. 2022; Fernández-Ponce et al. 2021; Huang et al. 2022). As a crucial modulatory factor, IGFBP3 potentially exerts a crucial function in BP, such as cell proliferation, differentiation, and migration, hence holding significant importance in the repair of STI (Chao et al. 2021; Teufelsbauer et al. 2019).

Enabling genome and transcriptome sequencing and analysis at the single-cell scale, single-cell RNA sequencing (scRNA-seq) stands as a prominent high-throughput technology (Kalisky et al. 2011). It is adept at pinpointing specific cellular subgroups and revealing changes at the cellular level. The approach becomes essential in investigating genetic diversity in higher organisms, especially in disciplines like oncology, embryogenesis, and nerve studies (Wang et al. 2023; Pozojevic and Spielmann 2023; Chang et al. 2024). scRNA-seq sequencing analysis can reveal cellular heterogeneity, intercellular communication, and dynamic changes during STI, providing essential information for a deeper understanding of STI repair mechanisms and the development of novel treatment approaches (Sun et al. 2022; Cherief et al. 2022).

Hydrogels have significant applications in biomedicine, especially in tissue engineering and drug delivery systems, and stand out as a top contender for alternative materials, boasting impressive fluid absorption capabilities and a structure reminiscent of soft tissues (Ali et al. 2022; Huang et al. 2017). The utilization of three-dimensional (3D) printing technology enables the controlled fabrication of biomedical scaffolds. Compared to traditional heat-sensitive 3D printing, the amalgamation of 3-dimensional printing with live cellular structures or other bioactive components (including growth agents, pharmaceuticals) during 3D biological printing aims to generate supportive structures for tissue rehabilitation and regeneration, and has been widely applied in STI repair treatments (Chen et al. 2022; Li et al. 2023).

While constructing ADSC-IGFBP3 peptide self-assembling hydrogel scaffolds using 3D bioprinting technology to study their role in soft tissue repair has been reported, further confirmation of their effects and potential molecular mechanisms remains unclear. The objective of this research is to thoroughly investigate the molecular pathways of IGFBP3 protein in ADSCs cells during the repair of STI and to verify its function. By deeply investigating the specific mechanisms of action of IGFBP3 in the repair process of STI, this investigation seeks to lay down a scholarly groundwork for the recognition of fresh treatment goals and tactics, fostering the care and restoration of STI patients. Through the in-depth exploration of this study, valuable perspectives may offer guidance for subsequent advancements in the development of enhanced treatments for STIs, potentially resulting in positive impacts in clinical practice, enhancing patients'quality of life, and advancing the field of medicine.

Materials and methods

Ethical considerations in animal research

The investigation dutifully complied with the ethical standards and guidelines on conducting experiments with animals. Authorization for conducting all experimental protocols was granted by the Institutional Animal Care and Use Committee (IACUC) at our facility (Review number: KT20240661). Each creature was provided housing and attentive care following ethical guidelines, with experiments designed to reduce suffering. Upon the experiments'conclusion, euthanasia in a humane manner was performed on all nude mice under the effects of ether anesthesia.

Establishment of an STI mouse model

Adult BALB/c nude male mice (409, sourced from Vital River Laboratory Animal Technology Co., Ltd., located in Beijing, China) at 6–8 weeks old and weighing 18–25 g were accommodated in an animal facility following SPF standards. This facility maintained a 12-h light–dark rhythm, humidity levels at 60%− 65%, and temperature within 22–25 °C, with free availability of food and water. The mice underwent a one-week acclimatization period before the commencement of the trial, during which their physical condition was evaluated. The animal ethics committee at our institution has sanctioned the experimental protocol and the procedures for handling animals. Before the surgery, an O_2 mixture was used in conjunction with 2% isoflurane (1 L/min, R510 - 22–10, RWD Life Science, Shenzhen, China) to deeply anesthetize the mice. Once fully anesthetized, the surgical region underwent comprehensive sterilization applying 70% ethanol. A linear incision of approximately 7.0 cm in length was made along the midline of the mouse's back, parallel to the spine, with the depth controlled to the subcutaneous tissue without affecting the muscle layer. Following the incision, the skin was sutured using 5–0 absorbable sutures (VCP310H, Ethicon, USA). Postoperatively, mice were placed in pre-warmed recovery cages until fully awake. All mice received appropriate care post-surgery, including pain management and monitoring for any abnormal behavior or health issues (Yi et al. 2022).

Sample preparation for sequencing

Soft tissue from the wound of mice was obtained by surgical excision and disrupted. The tissue was digested at 37 °C in a solution of DMEM (11,965,092, Thermo Fisher, USA) encompassing 1 mg/mL of collagenase (C2674, Sigma-Aldrich, USA), 1 unit/mL of DNase I, and 10% FBS for 30 min. The filtrate, in combination with residual tissue, underwent filtration using a 200-mesh strainer, followed by centrifugation at 4 °C for 5 min (50 × g). The supernatant was then eliminated, and the cellular material was re-suspended in a complete DMEM medium, undergoing two subsequent washes. Application of red blood cell lysis buffer (C3702 - 120 ml; Beyotime, Shanghai, China) was employed to eliminate red blood cells. Apoptotic and dead cells were eliminated using a dead cell removal kit for membrane-bound proteins (17,899, StemCell Technologies, Canada) and immunomagnetic cell separation. The obtained cells were precipitated and resuspended in PBS to obtain the sequencing sample. The prepared sequencing samples were evaluated for cell viability and integrity and quantified through a microscope and flow cytometer (Leale et al. 2022).

scRNA-seq and data analysis

Qualified samples were acquired through the C1 single-cell automated preparation system (Fluidigm, Inc., South San Francisco, CA, USA) to gather singular cells. Subsequent cell trapping, mRNA was released and transcribed into cDNA within the chip. Initial pre-amplification of the transcribed cDNA occurred within a microfluidic chip in readiness for subsequent sequencing. The amplified cDNA was applied in fabricating libraries and underwent single-cell sequencing on the HiSeq 4000 Illumina platform (parameters: paired-end reads, read length 2× 75 bp, around 20,000 readings per individual cell).

The examination of data was executed through the application of the"Seurat"package within the R software. A quality control standard was applied by filtering out genes with $200 < \text{nFeature\_RNA} < 5000$ percent.mt < 20, consequently pinpointing the foremost 2000 genes displaying remarkable diversity. Performing principal component analysis (PCA) on the highly variable top 2000 genes was undertaken to lower the complexity of the scRNA-Seq dataset. Twenty primary components (PCs) were specifically picked for further analysis by utilizing the Elbowplot feature in the Seurat software package. The identification of main cell subtype clusters was achieved by employing the FindClusters function in Seurat, utilizing a resolution parameter set to 1. Subsequently, application of the t-distributed stochastic neighbor embedding (tSNE) algorithm facilitated the nonlinear reduction of dimensions in the scRNA-seq dataset. CellMarker online tool was applied to annotate cells according to the expression of lineage-specific marker genes identified by the Seurat package. Utilizing the"CellChat"module within the R software, an evaluation of cell communication dynamics was executed. The scRNA-Seq dataset underwent differential gene expression analysis applying the"Limma"package implemented in the R programming environment, selecting differentially expressed genes (DEGs) between different samples based on $|\log2\ FC| > 1$ and P.value < 0.05 (Fig. S1) (Ritchie et al. 2015; Leale et al. 2022).

High-throughput transcriptome sequencing

Validation of RNA Purity and Integrity: Assessment of RNA sample concentration was executed with the Nanodrop ND- 1000 spectrophotometer (Thermo Fisher) through the measurement of the OD260/280 ratio to confirm the absence of protein and organic contaminants. The Qubit RNA analysis kit (Q33221, Thermo Fisher, USA) was utilized to determine the RNA concentration. The following eligibility criteria were applied to the total RNA samples used in the successive investigations: RNA Integrity Number (RIN) ≥ 7.0 and a 28S:18S ratio ≥ 1.5.

CapitalBio Technology in Beijing, China generated and processed the sequence libraries. Each sample utilized a total of 5 μg of RNA. In brief, depletion of ribosomal RNA (rRNA) from the total RNA was executed through the Ribo-Zero magnetic kit (MRZG12324, Epicenter, USA). Subsequently, an Illumina-based approach involved utilizing the NEB Next Supreme RNA library prep kit (E7760S, NEB, USA) for the establishment of the sequencing libraries. The RNA underwent fragmentation, resulting in about 300 base pair (bp) segments within the NEB Next first-strand synthesis reaction buffer (5x). Generation of the first-strand cDNA was initiated by reverse transcriptase and random primers, followed by the synthesis of the second-strand cDNA in NEB. Next, the dUTP Mix is a key component found in the second-strand synthesis reaction buffer (10x). The cDNA fragments experienced end mending, polyadenylation, and adaptor ligation. After ligating the Illumina sequencing adapters, the cDNA’s second strand underwent digestion by the USER Enzyme (M5508, NEB, USA) for the creation of strand-specific libraries. The library DNA underwent a process of amplification, purification, and enrichment through PCR. Subsequently, Agilent 2100 was utilized for the assessment of the library, while the quantification of its content was accomplished by employing the KAPA library quantification kit (kk3605, Merck, USA). Finally, the Illumina NextSeq CN500 sequencing platform was utilized for paired-end sequencing (Fig. S1) (Méar et al. 2024; Nynca et al. 2023).

Transcriptome sequencing data analysis

FastQC software v0.11.8 was employed to appraise the quality of the paired-end reads from the primary sequencing data. Initial data preparation involved the utilization of Cutadapt software 1.18 to eliminate both Illumina sequencing adapters and poly(A) tail sequences. Filtered out content with an N content surpassing 5% through a Perl script. Implementation of FASTX Toolkit v0.0.13 allowed the retrieval of sequences with a base quality exceeding 20 and including 70% of the total bases. The use of

BBMap software enabled the fixing of the paired-end sequences. Subsequently, the screened superior read fragments were mapped to the mouse reference genome through the application of hisat2 tool (version 0.7.12) for alignment evaluation.

Assessing differential mRNA read count expression was done utilizing the"Limma"software package in R programming, with the criteria set as $|\log2\ FC| > 1$ and P-value < 0.05. The identification of overlapping genes was achieved by conducting Venn diagram analysis with the assistance of the"VennDiagram"package implemented in the R language. Through the application of the R programming language's"ClusterProfiler"toolset, an investigation into the overlapping genes was executed to carry out Gene Ontology (GO) functional enrichment analysis, including analyses of biological processes (BP), molecular functions (MF), and cellular components (CC), followed by the visualization of GO enrichment results in bubble and circle plots. Employing $|\log2\ FC| > 1$ as the selection criterion, the utilization of the"ClusterProfiler"suite within the R programming platform enabled the performance of Kyoto Encyclopedia of Genes and Genomes (KEGG) enrichment analysis for the putative target genes, presenting the results in visual format through bubble and circular plots (Nynca et al. 2023; Galbo et al. 2021).

Exploring the GeneCards database (https://www.genecards.org/) allowed for the retrieval of genes linked to STI by conducting a search using the term"soft tissue injury,"ultimately revealing 5529 genes related to STI. The intersection of this gene set with the DEGs of ADSCs and high-throughput transcriptome sequencing data was then analyzed employing the"VennDiagram"package in R language to identify genes significantly associated with STI and ADSCs (Stelzer et al. 2016).

Extracting and identification of ADSCs in mice

Obtaining and Culture of ADSCs: Following the euthanasia of BALB/c nude mice, subcutaneous adipose tissue was collected using liposuction, and 150 mL of fat aspirate was minced in PBS. Subsequently, the tissue was digested in 0.075% collagenase I (17,100,017, Thermo Fisher, USA) at 37.0 ℃ with continuous agitation for approximately 45 min. The digested tissue was then washed in modified DMEM/F12 (12,634,010, Thermo Fisher, USA) enriched with 10% FBS (10100147 C, Thermo Fisher, USA) containing Dulbecco's Phosphate-Buffered Saline (DPBS). The pellet enriched with cells post-centrifugation at 600 ×g, 25 ℃ for 5 min, was reconstituted in PBS, ran through a wash cycle, and subjected to dual centrifugation at 500 ×g, 25 ℃ for 5 min per round. Following suspension in DMEM medium (11,965,092, Thermo Fisher, USA) enriched with 10% FBS and 2% penicillin–streptomycin (100 U/mL penicillin and 100 μg/mL streptomycin, 15,140,163, Thermo Fisher, USA), cell enumeration was performed, and the cells were introduced into a 100 mm culture dish at a density of 5×10^6. The medium was changed for the first time after 36 h post-seeding and subsequently every 72 h. Passaging was executed upon reaching 80–90% cell confluence using trypsin with ethylenediaminetetraacetic acid (Gibco); the second passage of ADSCs was cryopreserved. Cells were not used beyond the sixth passage (Song et al. 2023; Khazaei et al. 2021).

Identification of ADSCs: The third passage of ADSCs was harvested and washed three times in PBS. The cell suspension was subsequently placed in a dark environment at a temperature of 37.0 degrees Celsius for half an hour with antibodies against CD44, CD105, CD34, and CD45 (catalog numbers: ab243894, ab221675, ab81289, ab25386, diluted 1:500, all purchased from Abcam, UK). Post incubation, the cells underwent cleansing, were resuspended in PBS, and were examined for surface marker expression using the FACSCalibur System (USA). The positive expression of CD44 and CD105 (mesenchymal stem cell markers) and negative expression of CD34 (hematopoietic stem cell marker) and CD45 (blood cell marker) were confirmed (Song et al. 2023).

Adipogenic Differentiation in Vitro: The third passage of ADSCs was cultured in DMEM comprising 10% FBS until reaching 80% confluence. Subsequently, the ADSCs were inoculated into standard 6-well tissue culture dishes with 1.5×10^5 cells per well. These cells were induced to differentiate into adipocytes using the Mouse Adipose Mesenchymal Stem Cell Adipogenic Induction Medium (PD- 027, Wuhan PunoDx Life Science and Technology Co., Ltd., China), replacing the original medium. Cell cultivation lasted a total of twenty-one days, during which the solution was revised every three days.

Following differentiation, the cells were secured with a PBS mixture including 4% formaldehyde (P0099, Beyotime, Shanghai, China) for 30 min, then rinsed with isopropanol, and afterward tinted with Oil Red O solution for 30 min to assess the generation of fat globules. Post-staining, the cells were rinsed with PBS three times and observed through an Olympus inverted microscope (from Japan) to study adipogenic differentiation and for documentation (Ren et al. 2019).

Osteogenic Differentiation in Vitro: Prior to conducting the osteogenic differentiation experiment, pre-treatment of the 6-well cell culture dishes involved applying a coating of 0.1% gelatin (C0316, Beyotime, Shanghai, China) to promote cellular adhesion. ADSCs were introduced to each well with 2×10^5 cells on the pre-treated plates and cultured in the Mouse Adipose Mesenchymal Stem Cell Osteogenic Induction Medium (PD- 025, Wuhan PunoDx Life Science and Technology Co., Ltd., China) replacing the initial medium. Cultivation of the cells lasted for a fortnight, during which the medium was exchanged every 3 days. After osteogenic differentiation, the fixation of the cells involved the treatment with 4% paraformaldehyde (PFA) for 30 min, then proceeding to stain them with alizarin red staining solution for an additional 30-min interval to assess the calcium deposition. Upon completion of staining, the cells underwent a triple PBS rinse and were evaluated for osteogenic differentiation outcomes utilizing an inverted microscope (Olympus, Japan) (Ren et al. 2019).

Epithelial Differentiation in Vitro: Cells were cultured in L-DMEM encompassing 10% FBS (PM150220, Wuhan PunoDx Life Science and Technology Co., Ltd., China) and enriched with 25 μg/mL EGF (Epidermal Growth Factor), 5 μg/mL ATRA (Retinoic Acid), 10 μg/mL ActA (Activin A), 5 μg/mL FGF (Fibroblast Growth Factor), 5 μg/mL insulin, 0.4 μg/mL hydrocortisone, and 20 μg/mL glutamine (catalog numbers: HY-P1960, HY- 14649, HY-P73241, HY-P7066, HY-P0035, HY-N0583, and HY-N0390, MedChemExpress, USA). Medium exchange transpired every 3 days, and subsequent to a 14-day cultivation period, cell appearance was observed using a phase-contrast microscope. Cells were collected, and the identification of CK18 and ZO- 1 mRNA and protein levels in epithelial cell differentiation was determined through RT-qPCR and Western blot (WB).

HaCaT cell culture

HaCaT cells were procured from the Cell Bank/Stem Cell Bank of the Chinese Academy of Sciences (SCSP- 5091, China) and fostered in DMEM (REF# C11995500BT, Gibco) encompassing 10% FBS (REF# 10,091,148, Gibco) and 1% antibiotics (penicillin and streptomycin, REF# 15,140,122, Gibco) at 37 °C with 5% CO_2 in an incubating setting.

RT-qPCR

Extracting total RNA from tissues and cells involved the utilization of the Trizol extraction kit (A33254, Thermo Fisher, USA) in the process. The corresponding cDNA was synthesized employing the reverse transcription kit (RR047 A, Takara, Japan). Utilization of the SYBR® Premix Ex TaqTM II kit (DRR081, Takara, Japan) facilitated the establishment of the reaction system. Subsequent RT-qPCR analysis for fluorescence quantification was carried out utilizing the ABI7500 real-time PCR machine from Thermo Fisher, based in the USA. The PCR schedule was arranged in this way: pre-denaturation at 95 ℃ for 30 s, followed by cycling with an initial denaturation at 95 ℃ for 5 s, annealing at 60 ℃ for 30 s (cycling for 40 times), followed by extension at 95 ℃ for 15 s, extension at 60 ℃ for 60 s, and a concluding extension at 90 ℃ for 15 s to establish amplification patterns. GAPDH served as the internal reference, and each RT-qPCR assay was executed in triplicate with three technical duplicates. Through the utilization of the $2^{-\Delta\Delta Ct}$ methodology, the experimental group underwent a comparison with the control group to ascertain the fold change in gene expression, calculated as follows: $\Delta\Delta Ct = \Delta Ct_{\text{experimental group}} — \Delta Ct_{\text{control group}}$, where $\Delta Ct = Ct_{\text{target gene}} — Ct_{\text{reference gene}}$. Ct symbolizes the cycle threshold at which the fluorescence signal reaches a set threshold, signifying logarithmic phase amplification (Li et al. 2017). Table S1 displays the primer sequences.

WB

For WB assessment, utilization of RIPA lysis buffer (P0013B, Beyotime, Shanghai, China) along with 1% Phenylmethanesulfonyl fluoride (PMSF) based on the guidelines provided by the manufacturer facilitated the extraction of cell and tissue proteins. Each sample's protein measure was determined applying a BCA protein assessment kit (P0011, Beyotime, Shanghai, China), set at 1 µg/µL, and heated at 100 °C for 10 min before being stored at − 80 °C. Gel electrophoresis was implemented with 8%− 12% SDS-PAGE gels, taking into consideration the size of the target protein bands. Each lane was filled with fifty micrograms of protein extracts, and the application of an unchanging electrical potential in the range of 80 V to 120 V was observed during the 2-h electrophoresis procedure. Subsequently, the proteins were relocated to PVDF filters (1,620,177, Bio-Rad, USA) through a wet transfer system operated at a constant current strength of 250 mA for a duration of 90 min.

Subsequent to the protein transfer process, the membrane received a block treatment with 5% skim milk in 1× TBST at room temperature (RT) for an hour, followed by three washes utilizing 1× TBST for 10 min per wash. Primary antibodies (Table S2) underwent an overnight incubation at 4 °C, followed by three washes in 1× TBST lasting 10 min each, and three more washes at room temperature lasting 5 min each. The membrane was then treated with an HRP-conjugated secondary antibody, either goat anti-rabbit IgG (ab6721, dilution 1:5000, Abcam, Cambridge, UK) or goat anti-mouse IgG (ab205719, dilution 1:5000, Abcam, Cambridge, UK) at RT for 1 h. After receiving an additional three rounds of 5-min washes with 1× TBST at RT, the membrane was placed in the ECL substrate solution (1,705,062, Bio-Rad, USA) for 60 s, surplus solution was then drained, and visualization of the membrane was conducted utilizing the Image Quant LAS 4000 C gel documentation system (GE Healthcare, USA). The relative levels of protein expression were calculated by normalizing the intensity of the target band against the housekeeping protein GAPDH as a loading standard for evaluating the relative protein expression levels (Li et al. 2017). Every examination was executed in triplicate trials.

Immunofluorescence staining

Mice were euthanized via excessive anesthesia, and a skin flap was excised from the implantation site for immunofluorescence analysis. Three washes with PBS for 2-min durations each were performed on cells or tissues, which were later fixed in methanol at − 20 °C for 30 min. Redundant methanol was expelled, followed by three 5-min PBS washes for the specimens. Subsequently, permeabilization of the specimens took place with 0.1% Triton X- 100 for a period of 15 min at RT, followed by three PBS rinses lasting 5 min each. Implementation of blocking involved BSA for a duration of 30 min, then primary antibodies, including CK18 (PA5 -95,416, Thermo Fisher, USA) at 1:100, ZO- 1 (MA5 -44,375, Thermo Fisher, USA) at 1:200, Ki67 (MA5 -14,520, Thermo Fisher, USA) at 1:300, CD34 (PA5 -89,536, Thermo Fisher, USA) at 1:200, α-SMA (PA5 -85,070, Thermo Fisher, USA) at 1:100, or F-actin staining reagent kit (ab112127, Abcam, UK) were introduced and allowed to react at 37 °C for 60 min. Consecutive PBS rinses lasting 5 min each were undertaken three times.

Next, the samples were exposed to FITC-conjugated goat anti-rabbit IgG (A- 11008, Thermo Fisher, USA) secondary antibody at 1:500 dilution at 37 °C in a shaded setting for 60 min, accompanied by three 3-min PBS rinses. A 10-min DAPI staining procedure was conducted, followed by three PBS washes to eliminate any leftover DAPI (C1002, Beyotime, Shanghai, China). Finally, 20 µL of mounting medium was applied for slide sealing. After the medium had dried, visual scrutiny and image documentation of specimens were conducted through a fluorescent microscope. Image evaluation was undertaken employing ImageJ Pro Plus 6.0 software, measuring the fluorescent coverage area under a 40 × magnification from six predetermined fields of view and deriving their average values (Li et al. 2017).

Lentivirus transduction

The utilization of lentivirus infection was employed for the purpose of gene overexpression or gene suppression in ADSCs, with the provision of lentivirus packaging services by Gene Engineering in Shanghai, China. The pHAGE-puro plasmid series and helper plasmids pSPAX2 and pMD2.G (Addgene, USA #118,692, #12,260, and #12,259, respectively) were used, along with pSuper-retro-puro plasmid series and helper plasmids gag/pol and VSVG (Addgene, USA #113,535, #14,887, and #8454, respectively) for lentivirus packaging. The constructed plasmids were co-transfected into HEK293 T cells (Bio- 72947, Beijing, Booway Biotechnology Co., Ltd.) applying Lipofectamine 2000 reagent (Thermo Fisher, USA #11,668,030). Post 48-h cultivation of cells, the supernatant was amassed, passed through a 0.45 μm filter to collect the virus-containing fraction, concentrated by centrifugation after 72 h, and the concentrated virus from two collections was combined and titered.

During the logarithmic phase, trypsin-digested cells were distributed into 6-well plates, with each well containing 1×10^5 cells, and then incubated for a period of 24 h. Upon achieving a cell confluence of roughly 75%, the culture medium containing the lentivirus particles (MOI = 10, effective titer about 5×10^6 TU/mL) and 5 μg/mL polybrene (Merck, USA #TR- 1003) was added for infection. Upon a 4-h nurturing period, an equal amount of fresh medium was introduced to diminish the polybrene level. The medium underwent alteration 24 h after the infection occurred. Stable cell line generation involved cell incubation in a medium containing 2 μg/mL puromycin (Gene Engineering, Shanghai, China #E607054). Throughout the experiments, the puromycin levels were elevated progressively in 2, 4, 6, 8, and 10 μg/mL increments to select for resistance and establish consistent cell line cultures. Cells were collected when no death was observed in the puromycin-containing medium, and WB and RT-qPCR assays confirmed the efficiency of knockdown. The silencing lentivirus sequences are detailed in Table S3, and the optimal silencing sequences were selected for further experimentation (Song et al. 2023; Li et al. 2017).

The grouping of cells was designated as: sh-NC ADSCs cells (control cells transduced with Igfbp3 silencing lentivirus), sh-Igfbp3 ADSCs cells (Igfbp3 silenced cells), oe-NC ADSCs cells (cells transfected with empty lentivirus), and oe-Igfbp3 ADSCs cells (Igfbp3 overexpressing cells).

Measuring cell viability through CCK- 8 analysis

The ADSCs cells in each group underwent digestion and resuspension, with a cell density set to 1×10^5 cells/mL, and positioned in 100 μL per well within a 96-well plate for traditional cultivation overnight. By adhering to the directives outlined in the CCK- 8 kit (C0041, Beyotime, Shanghai, China), the cells were processed, and the cell viability was gauged through the CCK- 8 evaluation after 12 h, 24 h, 36 h, and 48 h following culture. Throughout every examination, 10 μl of CCK- 8 detection solution got introduced, and upon completion of a 60-min incubation at 37 degrees Celsius within a 5% CO_2 incubator, the optical density at 450 nm was gauged employing a microplate spectrophotometer (Thermo Fisher Scientific, Waltham, MA, USA). Cellular proliferation velocity was derived through the use of the subsequent formula: Cell Proliferation Rate = (Absorbance of the experimental group—Absorbance of the blank control group)/(Absorbance of the control group—Absorbance of the blank control group) (Song et al. 2023).

EDU staining

Cultivated in a 24-well dish, ADSC cells were allocated at a rate of 1×10^5 cells per well, with three duplicate wells per group. Edu (5-Ethynyl- 2'-deoxyuridine) solution (ST067, Beyotime, Shanghai, China) was introduced into the culture medium to attain a 10 μmol/L concentration. The cells were then kept inside a cultivation chamber for 2 h. Subsequently, the culture medium was aspirated, and the cells were preserved by a PBS blend with 4% PFA at RT for 15 min. Post double rinses with PBS having 3% BSA, the cells were subjected to incubation with PBS that included 0.5% Triton- 100 for 20 min at RT. Subsequent to two more PBS washes with 3% BSA, 100 μL staining solution was delivered into each well, and the cells underwent incubation in the dimness at RT for a duration of 30 min. DAPI was subsequently introduced to color the cellular nuclei lasting 5 min. Post-mounting, examination was conducted on 6–10 fields selected randomly with the assistance of a fluorescence microscope (FM- 600, Shanghai Putian Optical Instrument Co., Ltd.), and the count of positive cells in every field was noted. The estimation of the Edu labeling percentage was conducted in the ensuing manner: Edu Labeling Rate = (Number of positive cells)/(Number of positive cells + Number of negative cells) × 100% (Song et al. 2023). Every test was reiterated thrice.

Transwell migration assay

After subjecting ADSCs cells to different treatments for 24 h, a Transwell migration assay was performed. The lower chambers of Transwell inserts were prewet with culture medium without FBS. The cell samples were thinned to a density of 2.5×10^4 cells/mL in FBS-deprived culture medium, and 100 μL of cellular mix was placed into the upper chamber of every well, whereas 500 μL of culture solution with 10% FBS was poured into the lower chamber. Post a 24-h duration, the inserts were taken out, and the cells above were eradicated with a cotton swab. Fixation of the cells was initiated with 4% PFA at RT for 30 min, then proceeded by staining using 0.1% crystal violet for an equal period of time. The cell number was calculated by observing five varied regions through an inverted microscope (IXplore Pro, Olympus, Japan) (Song et al. 2023). The examination was reiterated thrice.

Wound healing test

A scratch test was performed on a 6-part dish. Through the use of a measuring device and a marking tool, horizontal lines were drawn at intervals of 0.5–1 cm on the base of each well, with each well crossed by at least 5 lines. Each well of the 6-well plate was filled with 5×10^5 ADSCs for cell culture. When the cells reached confluence, a scratch was produced perpendicular to the hand-drawn lines using a 200 μL pipette tip. A serum-exempt medium was employed as an alternative culture setting, while the width of the wound gap was evaluated at both the outset and after 24 h utilizing an optical scope (DM500, Leica). Image acquisition via a reversed microscope facilitated the observation of cellular migration within diverse groupings. The scratch width was analyzed using Image-Pro Plus 6.0 software, and the velocity of wound healing was assessed by employing the formula explicated in a previous academic inquiry (Song et al. 2023).

$$Woundhealingrate = \frac{distance_{0h} - distance_{24h}}{distance_{0h}}$$

In this context, $\text{distance}_{0\ \text{h}}$ and $\text{distance}_{24\ \text{h}}$ represent the cell scratch width at 0 h and 24 h, respectively, post scratch initiation.

Co-immunoprecipitation experiment (Co-IP)

Cell lysis was carried out on ice for 10 min using IP lysis buffer (P0013, Beyotime, Shanghai, China) applying proteinase and phosphatase inhibitors. Subsequently, following centrifugation at 12,000 g for a time span of 20 min at a temperature of 4 °C, the supernatant preparations from the lysate were appropriately utilized in conjunction with the BCA protein estimation set to gauge the overall protein concentration present in each distinct specimen. The protein concentration was adjusted to 1 μg/μL. Equal amounts of protein (20 μg) were used as input and in the immunoprecipitation experiment. Protein G magnetic beads (10004D, Thermo Fisher, USA) were added along with 10 μL of anti-IGFBP3 (ab220429, Abcam, UK) or anti-ITGB1 (ab183666, Abcam, UK) diluted in PBS. The mixture was kept still overnight at 4 °C on a rocking platform. Post incubation, the samples were spun at 5000 ×g for a 5-min duration at 4 °C, the supernatant was decanted, and the immunocomplexes underwent four rounds of washing with NETN buffer (20 mM Tris, pH 8.0, 100 mM NaCl, 1 mM EDTA, and 0.5% NP- 40). The complexes were then separated through SDS-PAGE and subjected to WB analysis using specific antibodies (Song et al. 2023).

Preparation of Gel-PCL self-assembling hydrogel using high voltage electrospinning technology

Preparation of PCL Fiber Network: High molecular weight polycaprolactone (PCL, molecular weight of 70,000 to 90,000, P485966, Aladdin) underwent dissolution in a mixture of dichloromethane (494,453, Merck, USA) and N, N-dimethylformamide (DMF, HY-Y0345, MedChemExpress) in a volume ratio of 1:4 (v/v) at RT. Stirring with a magnetic stirrer was maintained for 6 to 8 h until complete dissolution of PCL was achieved, yielding a clear solution. Electrospinning was carried out using high-voltage electrospinning equipment (Electrospinner, Linari Engineering, Italy), and the PCL solution was continuously added at a constant flow rate using a syringe pump (Harvard Apparatus, USA). The electrospun PCL fiber network underwent a vacuum drying process in a Binder oven from Germany for more than 5 h to guarantee the total evaporation of the solvent.

Fiber Phase Separation Treatment: A mixed solution of N-hydroxysuccinimide (NHS, HY-D0802, Sigma-Aldrich, USA) and 1-(3-dimethylaminopropyl)− 3-ethylcarbodiimide hydrochloride (EDC, HY-D0178, Sigma-Aldrich, USA) was prepared in MES buffer (2-Morpholinoethanesulphonic acid, MES, HY-D0858, Sigma-Aldrich, USA) at a concentration of 0.1 mol/L. The electrospun PCL material was trimmed to the appropriate dimensions and immersed in the NHS/EDC solution for 20 min to promote surface crosslinking. Subsequently, the material was washed three times with physiological saline to remove unreacted crosslinkers.

Preparation of Self-Assembling Hydrogel: Elevated voltage electrospun materials were generated in a biphasic structure. The materials used were PCL (Mn = 70,000–90,000), gelatin (Gel, EFL-GEL- 001, Suzhou Intelligent Manufacturing Research Institute), and IGFBP3 protein (775-B3 - 025, Bio-Techne, USA); the solvent used was trifluoroethanol (TFE, T63002, Sigma-Aldrich, USA). A homogeneous liquid was prepared by mixing 2 g each of PCL, gelatine, and IGFBP3 in a mass ratio of 2:1:1, and introducing the blend into 10 mL of TFE followed by continuous agitation for 4 h at 40 °C until full dissolution. The resulting solution was then processed using a syringe pump for high-voltage electrospinning to prepare the self-assembling hydrogel IGFBP3-Gel-PCL (abbreviated as IGP), and a corresponding method was used to prepare the Gel-PCL hydrogel without IGFBP3 protein (abbreviated as GP).

Scanning Electron Microscopy (SEM) and Transmission Electron Microscopy (TEM) Analysis: Preceding and succeeding the phase separation intervention, the samples were immersed in a 2.5% glutaraldehyde solution (8.20603, Sigma-Aldrich, USA) for an entire night. Subsequently, the samples went through a progressive desiccation process involving diverse ethanol concentrations (30%, 50%, 70%, 90%, 100%), followed by treatment with n-butanol. The specimens were then desiccated employing the critical point desiccation technique and captured by an SEM (Hitachi, Japan) in vacuum mode (20 mA, 150 s). For TEM analysis, PCL fibers were directly prepared on copper grids and imaged using a TEM (Hitachi H- 7500, Japan) to evaluate the materials' microstructure and fiber phase separation effect (Xu et al. 2022).

Preparation of bio-ink and 3D bioprinting

Preparation of bio-ink involved the combination of self-assembling GP or IGP nano-peptide hydrogel with ADSCs as the bio-ink for 3D printed tissue models. ADSCs cells were collected post trypsinization, repeatedly resuspended in sterile IGP hydrogel to ensure even cell distribution, forming a single-cell suspension to obtain bio-ink either Gel-PCL@ADSCs (abbreviated as GPA) or IGFBP3-Gel-PCL@ADSCs (abbreviated as IGPA).

Utilization of Fourier Transform Infrared Spectroscopy (FTIR) and X-ray Diffraction (XRD) experiments facilitated the characterization of the bio-ink. The hydrogel was stored in a freezer set at − 20 ℃ prior to undergoing freeze-drying for a total duration of 48 h as part of the FTIR analysis. The freeze-dried sample (1 mg) was blended with 80 mg dried KBr (221,864, Sigma, USA), pulverized to a fine texture, and compacted into pellets. Utilizing an infrared analyzer (Nicolet 6700, Thermo Fisher, USA), the pellets were subjected to single-beam absorption scanning with specified parameters to capture the infrared spectra (resolution: 4 cm^{-1}, covering wavelengths from 4000–400 cm^{-1}, scanning speed: 0.15 cm/s, number of scans: 128, continuous purging of pure helium at 5 mL/min rate over the sample surface during scanning). XRD analysis involved placing the sample in an XRD instrument (SmartLab- 9 kW, Rigaku, Japan) for measurement at RT. The scanning angle range was set from $2\theta = 10°$ to 80° to cover most crystalline material characteristic diffraction peaks. The scan rate was controlled at 3°/min to ensure sufficient resolution while avoiding lengthy testing times. A Cu Kα radiation source ($\lambda = 1.5418$ Å) was utilized for clear diffraction patterns. Following XRD data collection, data processing and analysis were performed using Rigaku's specialized software.

In 3D bioprinting, the prepared bio-ink was loaded into the cartridge, stored at RT for 15–20 min, and then injected into the bioprinting machine (Axolotl BIOSYSTEMS, AXO A3) nozzle. Quartz glass coverslips were sterilized before use, and all experiments were conducted aseptically on a clean bench. Bioprinting parameters were set as follows: nozzle diameter of 23 G (0.60 mm), injector and nozzle temperature set at 37 ℃, printing bed temperature at 8 ℃, print head moving speed at 4–5 mm/s, and extrusion pressure at 10–20 kPa. The cell-laden hydrogel was punched into discs (diameter 6 mm × thickness 1 mm), and after bioprinting, the resulting 3D structures were cultured in a complete medium at 37 ℃ and 5% CO_2 until further experimentation. Repetition of the experiment three times led to the formation of a consistent bio-ink imbued with cells.

Contact angle analysis was conducted using circular samples measuring 8 mm in diameter and 3 mm in height prepared from different bio-inks, crosslinked under 405 nm UV light. Wetting properties were tested using a Pioneer contact angle goniometer (located in Succasunna, New Jersey, USA) with distilled water, with each group undergoing three repetitions.

Swelling Ratio and Degradation Rate: The swelling ratio was determined by preparing circular samples sized at 8 mm in width and 3 mm in thickness using bio-ink of different concentrations crosslinked under 405 nm UV light. Specimens underwent a soaking process in PBS at 37 ℃ for 12 h and weighed to obtain M1; subsequently, they were freeze-dried for 12 h and reweighed to obtain M2. Utilizing the formula Qs =M1/M2 allowed for the determination of the swelling ratio Qs. Experimental degradation procedures involved placing the test items in a 24-well container filled with degradation solution incorporating 0.5 mg/mL of collagenase I (1,148,089, Sigma-Aldrich, USA). Collections from distinct time points were gathered, underwent freeze-drying, and the weight was determined, indicated as mass (Wr). The primary quantity W0 representing the sample size, with the degradation rate Qd determined by the ratio Wr/W0. Every distinct experimental set was executed three times independently.

Compression Test: Samples in circular shape, 8 mm wide and 3 mm high, were generated utilizing bio-ink solutions of diverse concentrations for the intent of compression assessment. A 20 g load cell sensor was utilized on a universal testing machine (CMT1000, Sansi Technology) to perform the compression tests. The samples were compressed at a velocity of 0.01 mm/s up to a final strain of 30%. The compression modulus was obtained by calculating the slope in the linear range of 2%–10% strain. This process was repeated three times for each experimental group to ensure reliability.

Assessment of cell viability

Following 3D bioprinting, Calcein AM (C3099, Thermo Fisher, USA) and Propidium Iodide (PI) (DN1005 -010, innibio, USA) were utilized for the differentiation of living and non-living cells. Cell cultures were maintained in a solution comprising 1 μM Calcein AM, subsequently exposed to a temperature of 37 ℃ for 30 min, and rinsed thrice with PBS. Subsequently, cell samples were cultured in a solution comprising 1 μM PI for a 10-min period, then subjected to three rounds of washing using PBS. Capturing was executed utilizing a confocal microscope (Carl Zeiss AG, Germany, model 880) to acquire unique visuals from diverse angles. Testing was executed on three different sets, and cell vitality was determined with the aid of ImageJ program (Xu et al. 2022).

Furthermore, cells were treated following the prescribed protocol of the CCK- 8 analysis kit (C0041, Beyotime, Shanghai, China). Upon 48 h of cultivation, cell viability was determined through the CCK-8 assay. During each assay, 10 μl of CCK- 8 reagent were introduced, subsequently undergoing a 4-h incubation process in the cell culture incubator. The determination of cell viability involved measuring the absorbance at 450 nm with a microplate reader (Baka et al. 2023).

In vivo animal experiment

From Beijing Vital River Laboratory Animal Technology Co., Ltd. in China, eighteen male BALB/c nude mice, aged 6–8 weeks and weighing 18–25 g, were procured for the study. Every mouse was accommodated at an SPF-class animal testing location featuring regulated illumination (12 h of light followed by 12 h of darkness), humidity maintained at 60%– 65%, and temperatures set between 22–25 ℃, and was offered unrestricted food and water intake. Upon completion of a one-week acclimation period, an assessment of the mice's physical condition was undertaken prior to the initiation of the study. The Institutional Animal Ethics Committee has granted approval for the experimental protocol and procedures involving animals.

The division led to the creation of three groups, with six mice in each group: the GP group (treated with GP hydrogel), the GPA group (treated with GPA hydrogel), and the IGPA group (treated with IGPA hydrogel). In line with the previously stated protocol, a STI model was established in mice by creating a full-thickness skin wound measuring 7 mm in width along the midline of their backs. Following wound formation, different hydrogels were used for treatment. Photographs of the wound of each mouse were taken at fixed intervals of every 24 h for 14 days, on days 0, 3, 7, 10, and 13, and ImageJ-Pro Plus 6.0

software was used to compute the area of the wound (Yi et al. 2022).

Hematoxylin and eosin (H&E) staining

Utilizing the hematoxylin and eosin staining kit (C0105S, Beyotime, Shanghai, China), the H&E staining process was implemented. Preservation of tissue samples involved the use of 4% PFA for fixation, dehydration, and paraffin embedding. Slices that were 5 µm thick underwent cutting procedures with a microtome, followed by baking, dewaxing to water, hematoxylin staining, rinsing with distilled water, immersion in 95% ethanol, eosin staining, differentiation in 70% hydrochloric acid ethanol, dehydration, clearing in xylene, and mounting with neutral resin. Slide preparation was completed, and tissue morphological changes were identified through optical microscope observation (Yi et al. 2022).

Masson staining

Utilization of the Masson trichrome staining kit (DC0032, Leagene Biotechnology, Beijing, China) enabled the performance of Masson trichrome staining. Slices measuring 4 µm in thickness underwent dewaxing to water, were tinted with hematoxylin for 5–10 min, underwent differentiation in acidic ethanol lasting 5–15 s, received a water rinse, were immersed in Masson blue solution for 3–5 min, were subsequently rinsed, incubated in ponceau fuchsin for 5–10 min, underwent washing in phosphomolybdic acid solution for 1–2 min, underwent staining with aniline blue solution for 1–2 min, were dehydrated using ethanol, clarified with xylene, and finally positioned for viewing. Assessment of collagen fiber area ratios involved the quantitative analysis of randomly selected visual fields, with a minimum of three fields at 200 ×magnification using an Olympus BX51 microscope (Tokyo, Japan). Assessing collagen fiber deposition was facilitated by the ImageJ-Pro Plus 6.0 image analysis tool (Xu et al. 2022).

Immunohistochemical staining

The methodology involved cooling the paraffin on ice or in a refrigerator at 4 °C, followed by embedding the slices. Upon completion of the air-drying process for the paraffin-embedded slices, the slides were exposed to 60 °C heat in an oven for a duration of 20 min. Submerging them in xylene for 10 min, alternating xylene and immersing for a further 10 min was the next step undertaken with the sections. The next stages comprised immersion in absolute ethanol for 5 min, succeeding with additional immersion steps and immersion in alcohol solutions of 95% and 70% for 10-min intervals each, concluding with a final rinse in distilled water lasting 5 min. The slices were then subjected to antigen retrieval by immersing them in citrate buffer (pH 6.0) and heating them on high in a microwave for 8 min, then allowed to cool down to RT. Subsequent washes with PBS (pH 7.2–7.6) were done three times, each for 3 min. The deactivation of endogenous enzymes was achieved by adding 3% H_2O_2 and letting it stand at RT for 10 min, trailed by three successive 3-min washes employing PBS. The slides were then blocked with normal goat serum blocking solution (E510009, from Sino Biological, Shanghai, China) at RT for 20 min.

Subsequent to the incubation period, specific primary antibodies against IGFBP3, ITGB1, CK18, ZO- 1, and PCNA (catalog numbers: ab217205, ab183666, PA5 -95,416, MA5 -44,375, and ab92552, dilutions: 1:100, 1:500, 1:100, 1:100, and 1:500 respectively, from Abcam, UK or Thermo Fisher, USA) were included on the slides and incubated overnight at 4 °C. The slides underwent three rounds of PBS washing, followed by exposure to secondary antibody goat anti-rabbit IgG (ab6721, concentration: 1:5000, Abcam, Cambridge, UK) for half an hour. Subsequently, SABC (P0603, Beyotime, Shanghai, China) was applied at 37 °C for 30 min within a constant temperature chamber. DAB chromogenic reagent (P0203, Beyotime, Shanghai, China) was applied for staining purposes. It involved the addition of a single droplet onto the specimen, a 6-min incubation period, subsequent counterstaining with hematoxylin for 30 s, and dehydration through a series of ethanol dilutions (70%, 80%, 90%, 95%, and absolute ethanol) with each step lasting 2 min. Finally, after immersion in xylene twice, each for a duration of 5 min, the slides were sealed with neutral resin to facilitate examination and analysis through a brightfield microscope (BX63, Olympus, Japan). Observation entailed the random selection of five high-powered fields on each slide, and the software Image-Pro Plus 6.0 was employed to assess the mean optical density observed in the images (Yi et al. 2022). The examination was reiterated thrice per sample.

Data analysis

Information was acquired from a minimum of three independent trials and is exhibited as mean ± standard deviation (Mean ± SD). The independent t-test was employed for the purpose of contrasting the two groups, while a one-way ANOVA was utilized for comparisons among three or more groups. When the ANOVA findings indicated noteworthy distinctions, successive evaluations utilizing Tukey's Honestly Essential Discrepancy (HSD) post-hoc inspections were conducted to assess deviations between individual groups. In cases of non-normal distributions or heteroscedasticity, the Mann–Whitney U test or Kruskal–Wallis H test was used. Statistical methodology was applied incorporating GraphPad Prism 9.5.0 software (GraphPad Software, Inc.) and R version 4.2.1 (R Foundation for Statistical Computing). A significance threshold of 0.05 was utilized for all examinations, where a two-way p-value below 0.05 was classified as statistically notable, while quantities above 0.05 were designated as not statistically important.

Results

Cellular heterogeneity and cell type analysis in STI

To explore more effective therapeutic strategies for STI and promote rapid recovery and functional restoration after STI, we surgically established a STI mouse model. scRNA-seq investigation was executed on injured soft tissue (STI, n = 1) and normal soft tissue (control, n = 1). By integrating the data applying the Seurat package, we initially explored gene numbers (nFeature_RNA), mRNA molecule counts (nCount_RNA), and the percentage of mitochondrial genes (percent.mt) in every cell within the scRNA-seq data. The outcomes revealed that the vast majority of cells displayed nFeature_RNA < 5000, nCount_RNA < 20,000, and percent.mt < 20% (Fig. S2A). We excluded poor-quality cells by applying the standards of 200 < nFeature_RNA < 5000 percent.mt < 20%, leading to a total of 15,489 genes and 16,293 cells in the expression matrix. Correlation analysis of sequencing depth revealed a correlation coefficient of r = − 0.04 between nCount_RNA and percent.mt, and r = 0.89 between nCount_RNA and nFeature_RNA in the filtered data (Fig. S2B), signifying the quality of the refined cell data for subsequent analysis.

Further examination of the filtered cell population entailed the identification of markedly different genes through assessing gene expression diversity, culminating in the selection of the foremost 2000 diverse genes for subsequent investigation (Fig. S2C). Utilization of the CellCycleScoring function allowed for the calculation of cell cycle phases (Fig. S2D), and preliminary data normalization was performed. Post the selection of the specific highly variable genes, PCA was utilized to conduct linear dimensionality reduction. Here, we present the gene expression heatmap for PC_1 – PC_6 (Fig. S2E) and the distribution of cells in PC_1 and PC_2 (Fig. S2F), revealing the presence of batch effects among samples.

Batch effects were corrected using the harmony package to reduce such effects and enhance more accurate cell clustering (Fig. S2G). Additionally, utilization of an ElbowGraph helped in prioritizing the deviations of standard PCs, revealing that PC_1 through PC_30 effectively embraced the details derived from the specifically chosen highly diverse genes, portraying substantial analytical significance (Fig. S2H). The amended results exhibited the accomplished elimination of batch effects (Fig. 1A-B).

Later, the TSNE algorithm was deployed to carry out nonlinear dimension reduction on the top 20 PCs, and the"clustree"package was utilized to display clustering under different resolutions (Fig. S3). With the application of TSNE clustering analysis, all cells were assorted into 30 specific cell clusters (Fig. 1C-D). Subsequently, acknowledged cell lineage-specific marker genes were retrieved from documented research, and cell annotation was carried out using the CellMarker online platform, leading to the recognition of 9 distinct cell categories: Endothelial cells, Adipocytes, Monocytes, ADSCs, Immune cells, Macrophages, Stromal cells, Bone cells, and Mesenchymal stem cells (MSCs) (Fig. 1E-F). Furthermore, the TSNE expression profiles of these 9 cell marker genes were displayed, with CD31 as the marker gene for Endothelial cells, Asc- 1 for Adipocytes, CD11b for Monocytes, Sca- 1 for ADSCs, Il10 for Immune cells, CD11c for Macrophages, CD13 for Stromal cells, Alpl for Bone cells, and CD105 for MSCs (Fig. 1G-H).

The aforementioned scRNA-seq analysis results demonstrate that samples from STI and normal soft tissue can be clustered into 30 clusters, successfully identifying 9 cell subtypes.

Multi-omics analysis reveals a close relationship between IGFBP3 expression level and the progression of ADSCs

The comprehensive examination in our study outlines the spatial distribution of 9 types of cells in 2 particular samples. The application of t-tests enabled the analysis of the discrepant levels of these cells in the control group and the STI samples. The analysis outcomes illustrate a substantial escalation in the number of ADSCs in the STI sample relative to the control sample (Fig. 2A).

Furthermore, to understand the functional differences behind these quantity variances, our investigation centered on ligand-receptor interactions in cell-to-cell signaling. Employing the R language'CellChat'package, we analyzed the communication and interactions of different cell phenotypes. The results demonstrate enhanced pathway connections between ADSCs and other cells in the STI sample in contrast with the control sample (Fig. 2B-E). These findings highlight the importance of ADSCs in the progression of STI. Additionally, the signaling pathways of the interaction between CAFs and other cells in the STI sample mainly include TGFβ1, H2, and LGALS9 signaling pathways (Fig. 2F-G). Collectively, these results underscore the role of ADSCs as crucial mediators of cell communication in STI (Mazini et al. 2020; Schneider et al. 2023; Tang et al. 2022).

To delve deeper into the function of ADSCs in STI advancement, a differential analysis of gene expression in ADSCs from normal soft tissue samples and STI samples was conducted, identifying 51 DEGs, with 27 genes significantly upregulated, and 24 genes significantly downregulated in the STI samples (Fig. 3A). Additionally, we executed high-throughput transcriptome sequencing (RNA-seq) on control samples (n = 3), and STI samples (n = 3), resulting in the identification of 347 DEGs, with 184 genes upregulated, and 163 genes downregulated (Fig. 3B).

The DEGs identified via RNA-seq were assessed for functional enrichment in the GO database, elucidating their participation in BPs including the production of molecular mediators of immune response, immunoglobulin production, and hormone secretion. In CC, they mainly enriched the collagen-containing extracellular matrix, postsynaptic membrane, and myofibril components. In terms of MF, they were primarily associated with growth factor activity, cell adhesion molecule binding, and carbohydrate-binding (Fig. 3C). Analysis of the DEGs'enrichment in KEGG pathways demonstrated their marked involvement in pathways like PI3 K-Akt signaling, neuroactive ligand-receptor interaction, calcium signaling, cytokine-cytokine receptor interaction, and MAPK signaling pathways (Fig. 3D).

To further identify key genes influencing the progression of STI, we obtained a set of 5529 genes related to"soft tissue injury"from the GeneCards database. We performed a Venn analysis by comparing this gene set with the 51 DEGs in ADSCs and the 347 DEGs from RNA-seq, resulting in the identification of a single DEG significantly associated with both STI and ADSCs—Igfbp3 (Fig. 3E). Moreover, in our single-cell t-SNE plot, we detected elevated levels of the Igfbp3 gene in injured soft tissue (Fig. 3F) and a noteworthy surge in its expression in ADSCs (Fig. 3G). Consequently, our theory revolves around the pivotal function of the Igfbp3 genetic factor in governing STI.

In conclusion, through integrated examination of scRNA-seq and RNA-seq, we preliminarily recognized ADSCs as key cells mediating cell communication in STI. The significant upregulation of Igfbp3 gene expression in ADSCs from injured soft tissue suggests its potential direct contribution to the physiological and pathological functions of STI.

IGFBP3 promotes ADSCs epithelial cell differentiation, proliferation, and migration

Through the integrated omics sequencing and bioinformatics analysis mentioned above, we have preliminarily identified Igfbp3 as a potential therapeutic target significantly associated with ADSCs during STI. To investigate the influence of the Igfbp3 gene on ADSCs'epithelial cell differentiation further, we isolated ADSC cells from mouse adipose tissue for in vitro culture (Fig. S4A). With prolonged

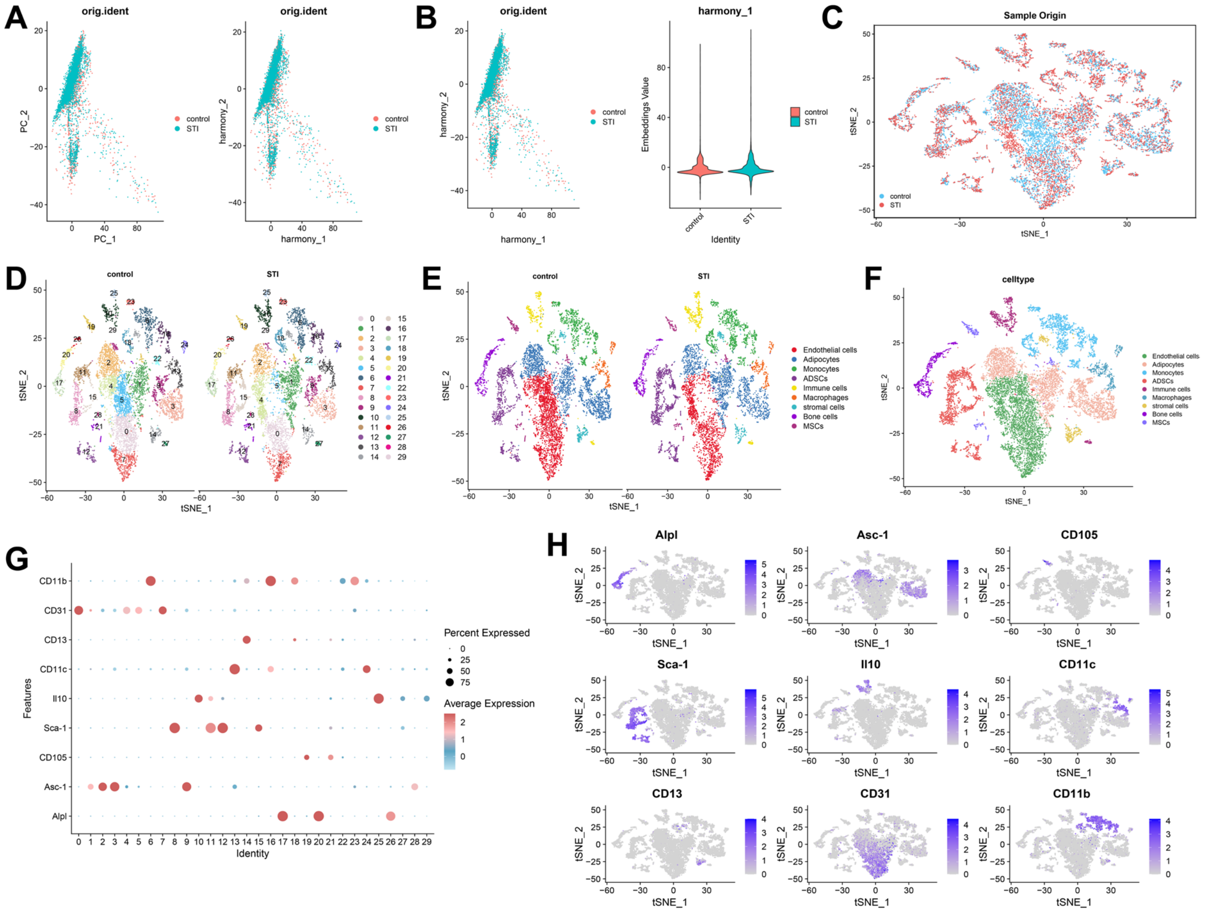

Fig. 1 Cell clustering in scRNA-seq data. Note: (**A**) Distribution of cells before (left panel) and after (right panel) batch correction with Harmony in PC_1 and PC_2, where each point represents a cell; (**B**) Distribution of cells after batch correction with Harmony in PC_1 and PC_2, where each point represents a cell; (**C**) Visualization of TSNE clustering results displaying the aggregation and distribution of cells from normal soft tissue sample (control, n= 1) and STI soft tissue sample (STI, n= 1) in two dimensions, where red indicates the STI sample and blue represents the normal sample; (**D**) Group visualization of TSNE clustering results showcasing the aggregation and distribution of cells from different source samples, with each color representing a cluster; (**E**) Visualization of cell annotation results grouping based on TSNE clustering, with each color representing a cell subtype; (**F**) Visualization of cell annotation results based on TSNE clustering, with each color representing a cell subtype; (**G**) Expression patterns of known lineage-specific marker genes in different clusters of normal tissue samples and STI samples, where darker red indicates higher average expression levels, and larger circles represent more cells expressing the gene; (**H**) Expression patterns of 9 cell marker genes in various cell subtypes, where darker blue signifies higher average expression levels

incubation, ADSCs gradually became homogeneous, forming a monolayer of adherent cells and exhibiting a typical fibroblast-like morphology (Fig. S4B). The characterization of the 3rd generation ADSCs using flow cytometry revealed strong positivity for CD44 (92.4%) and CD105 (99.1%) while being negative for CD34 (2.15%) and CD45 (2.62%) (Fig. S4C). Adipogenic and osteogenic differentiation assays were performed to assess the multipotency of ADSCs. After 3 weeks of adipogenic differentiation culture, the majority of cells displayed characteristics of adipocytes with Oil Red O staining (Fig. S4D). Similarly, alizarin red staining confirmed that after osteogenic differentiation culture, most cells differentiated into osteoblasts (Fig. S4E). These results demonstrate the effective extraction of ADSC cells from mouse adipose tissue.

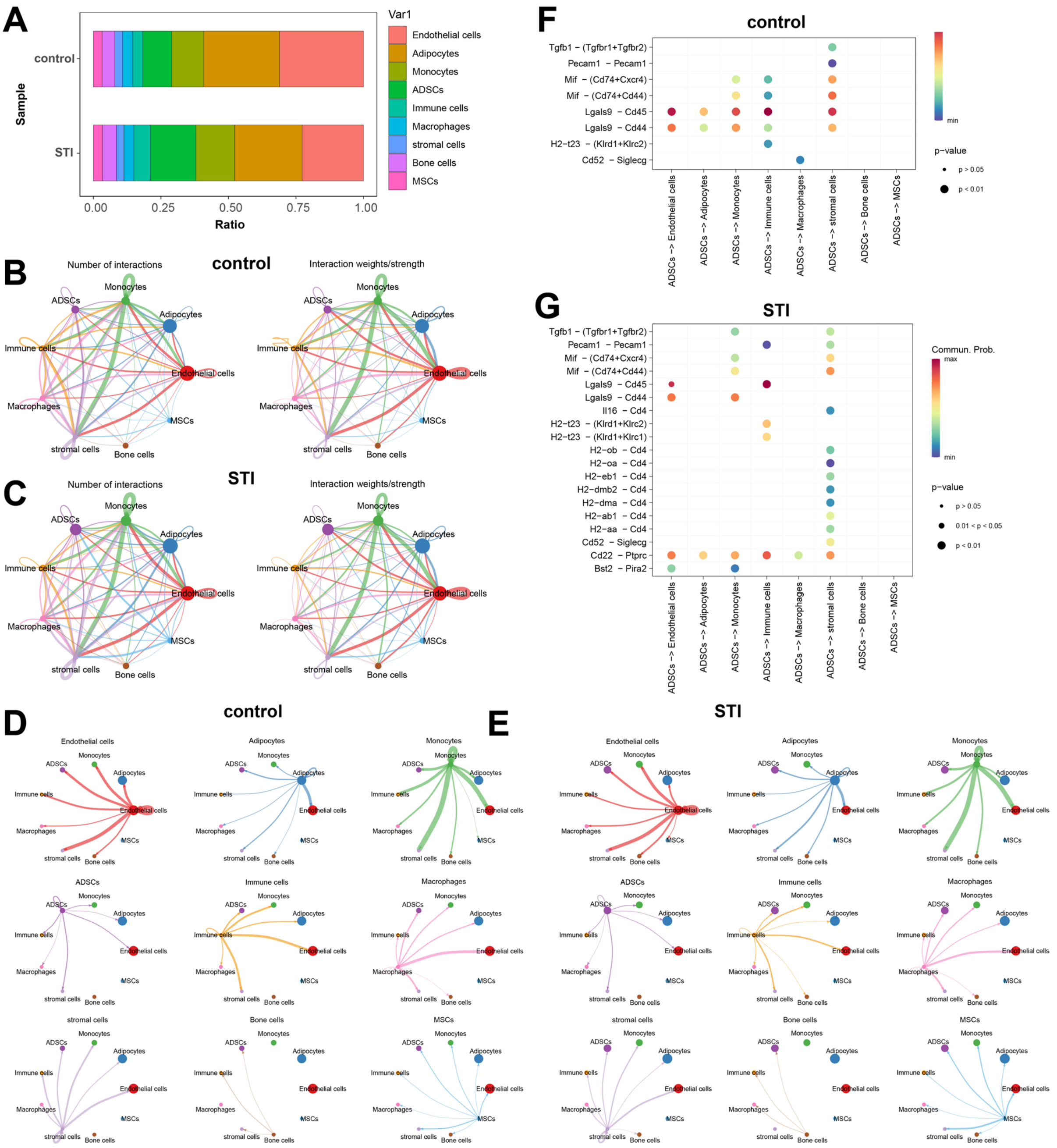

Fig. 2 Analysis of cell quantity discrepancies and cell pathways. Note: (**A**) Proportion of different cell subtypes in each sample, with different colors representing cell subtype types; (**B**-**C**) Interactome network diagrams in control and STI samples, with line thickness representing the number of pathways and intensity of interactions; (**D**-**E**) Interactome network diagrams of 9 cell types interacting with the other 8 cell types in control and STI samples, where line thickness denotes the number of pathways; (**F**-**G**) Bubble diagrams of the signaling pathways of ADSCs cells interacting with the other 8 cell types in control and STI samples

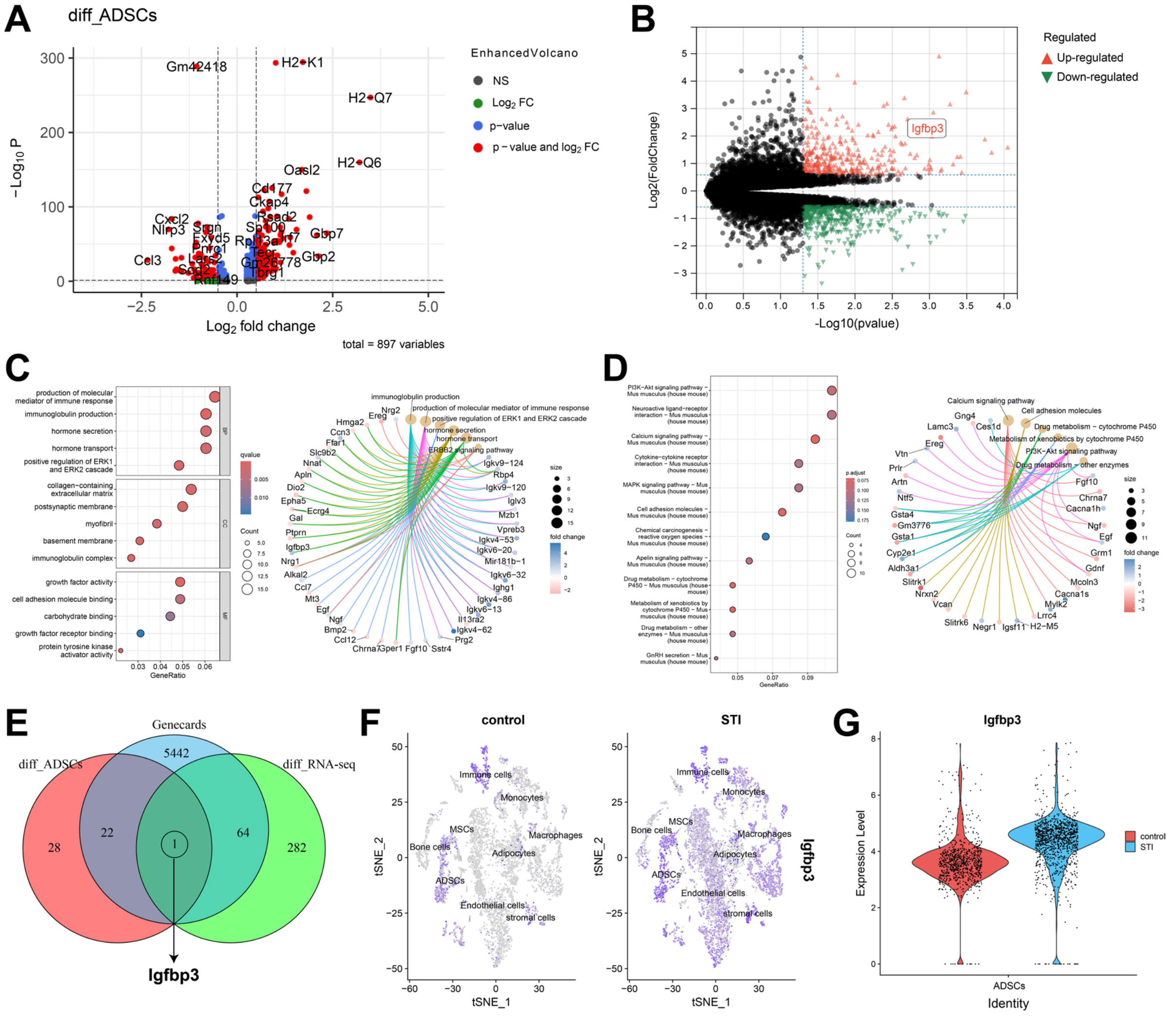

Fig. 3 Analysis of key genes in STI based on single-cell and transcriptome sequencing. Note: (**A**) Volcano plot showing DEGs between ADSCs cells from control and STI samples, with red dots left of the dashed line indicating genes highly expressed in the STI sample, and dots on the right showing genes with low expression in the STI sample; (**B**) Volcano plots of DEGs from 3 control and 3 STI samples in RNA-seq, with red triangles representing upregulated genes, green triangles denoting downregulated genes, and black circles indicating non-differential genes; (**C**) Bubble chart (left) and circular chart (right) of GO enrichment analysis of DEGs in RNA-seq, where the color of the circles represents the significance of enrichment from blue to red, and the size of the circles indicates the number of enriched genes; (**D**) Bubble chart (left) and circular chart (right) of KEGG enrichment analysis of DEGs in RNA-seq, with the color of circles indicating the significance of enrichment from blue to red, and the size representing the number of enriched genes; (**E**) Venn diagram of the intersection between DEGs in RNA-seq, scRNA-seq ADSCs, and Genecards dataset, leading to the identification of the key gene—Igfbp3; (**F**) scRNA-seq analysis of expression levels of Igfbp1 gene in control and STI samples, with blue indicating upregulation; (**G**) scRNA-seq analysis of expression of Igfbp3 gene in ADSCs cells from control and STI samples

For a more comprehensive evaluation of ADSCs'epithelial differentiation potential, we initially examined the cell morphology after induction with epithelial differentiation medium. Under an inverted microscope, it was observed that ADSCs without induction medium displayed elongated fibroblast-like morphology, while after induction for 14 days, ADSCs became shorter, smaller, and closer to an epithelial phenotype (Fig. S4F). Furthermore, RT-qPCR and WB analysis indicated a substantial

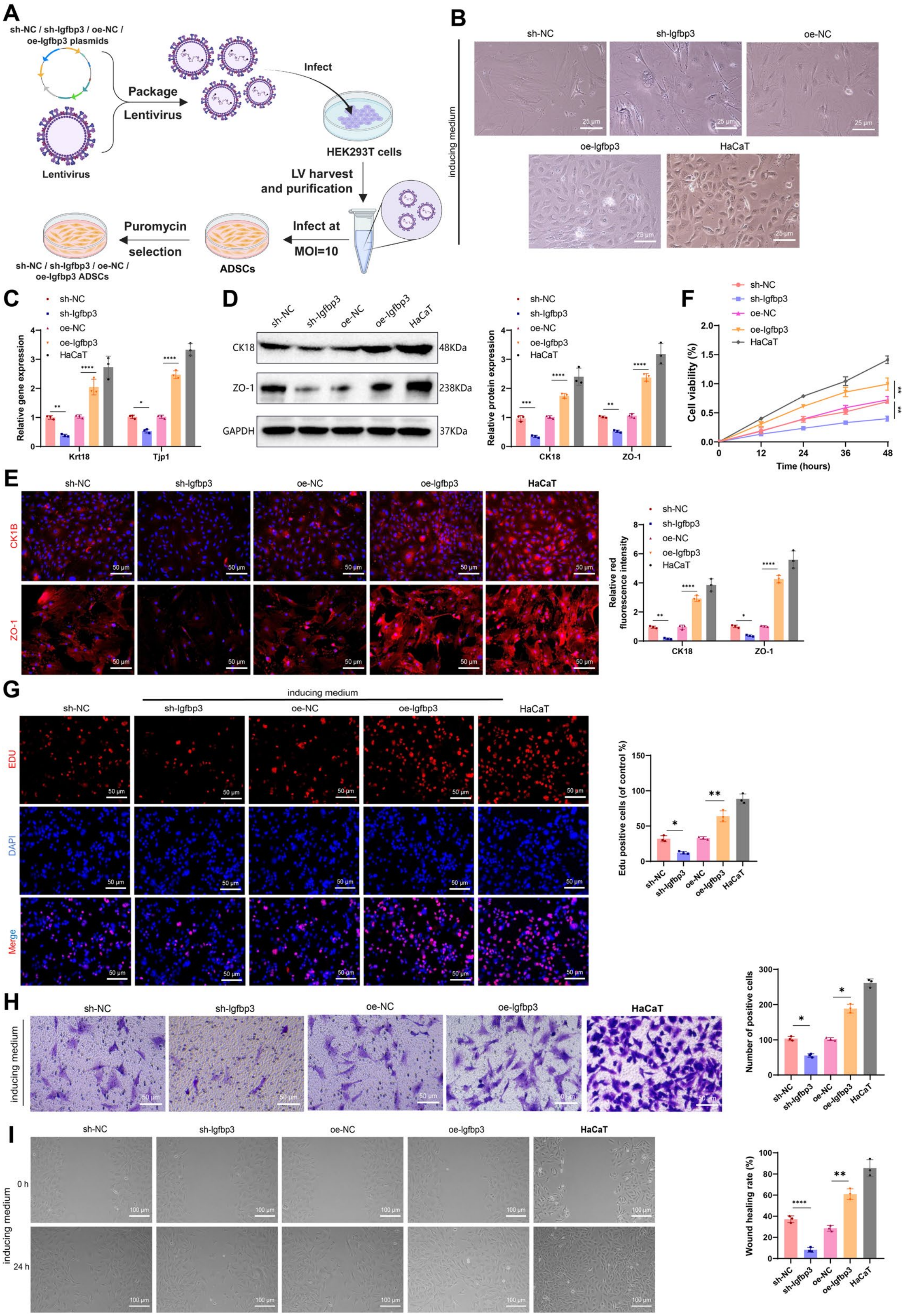
A
sh-NC / sh-Igfbp3 / oe-NC / oe-Igfbp3 plasmids
Package
Lentivirus
Lentivirus
Infect
HEK293T cells
LV harvest and purification
Infect at MOI=10
ADSCs
Puromycin selection
sh-NC / sh-Igfbp3 / oe-NC / oe-Igfbp3 ADSCs
B
inducing medium
sh-NC
sh-Igfbp3
oe-NC
oe-Igfbp3
HaCaT
25 μm
C
Relative gene expression
Krt18
Tjp1
D
CK18
ZO-1
GAPDH
48KDa
238KDa
37KDa
Relative protein expression
F
Cell viability (%)
Time (hours)
E
CK1B
ZO-1
50 μm
Relative red fluorescence intensity
G
inducing medium
EDU
DAPI
Merge
Edu positive cells (of control %)
H
Number of positive cells
I
0 h
24 h
100 μm
Wound healing rate (%)

◂**Fig. 4** Impact of IGFBP3 on ADSCs'epithelial cell differentiation, proliferation, and migration. Note: (**A**) Schematic diagram of the experimental process for Igfbp3 silencing or overexpression in ADSCs; (**B**) Observation of the effects of Igfbp3 silencing or overexpression on the morphology of ADSCs and the comparison with HaCaT cell morphology under an inverted microscope (scale bar =25 μm); (**C**) RT-qPCR detection of changes in Krt18 and Tjp1 mRNA expression in ADSCs after Igfbp3 silencing and overexpression, and expression levels in HaCaT cells; (**D**) WB detection of changes in CK18 and ZO- 1 protein expression in ADSCs after Igfbp3 silencing and overexpression, and in HaCaT cells; (**E**) Immunofluorescence staining for CK18 and ZO- 1 protein expression in ADSCs with different Igfbp3 interventions, and in HaCaT cells (scale bar =50 μm); (**F**) CCK- 8 assay detecting cell viability changes in ADSCs (with Igfbp3 interventions) and HaCaT cells at 12, 24, 36, and 48 h; (**G**) EDU assay detecting the proliferation capacity of ADSCs with Igfbp3 interventions, with EDU-positive cells shown in red (proliferating phase); blue indicates DAPI-stained cell nuclei (scale bar =50 μm); (**H**) Transwell assay detecting the migration ability of ADSCs with Igfbp3 interventions and comparison with HaCaT cells (scale bar =50 μm); (**I**) Scratch assay detecting the migration of ADSCs with Igfbp3 interventions and comparison with HaCaT cells (scale bar =100 μm). * indicates comparison between two groups, $**P < 0.01$, $***P < 0.001$, $****P < 0.0001$

upregulation of epithelial cell differentiation markers CK18 and ZO- 1 proteins and their encoding genes in ADSCs cells cultured with induction differentiation medium (Fig. S4G-H). Immunofluorescence staining of CK18 and ZO- 1 proteins further confirmed the potential of ADSCs cells for epithelial differentiation (Fig. S4I).

To delve deeper into the impact of Igfbp3 gene expression in ADSCs on epithelial cell differentiation and its specific regulatory mechanism, we constructed ADSCs cells with Igfbp3 overexpression and silencing through lentivirus transfection (Fig. 4A). The efficiency of Igfbp3 silencing or overexpression was validated via RT-qPCR and WB, and the cell line exhibiting superior efficiency was singled out for subsequent investigations (Fig. S5A-D). Inverted microscopy revealed that in epithelial differentiation-inducing medium, Igfbp3 silencing inhibited epithelial differentiation in ADSCs, while Igfbp3 overexpression promoted it, making the cells more similar to HaCaT epithelial cells (Fig. 4B). Data obtained through RT-qPCR and WB examination demonstrated that, in comparison with the control group, Igfbp3 silencing inhibited the expression of CK18 and ZO- 1 proteins and their encoding genes in ADSCs, whereas Igfbp3 overexpression significantly upregulated their expression, with levels approaching those of HaCaT cells (Fig. 4C-D). Immunofluorescence staining of CK18 and ZO- 1 proteins further demonstrated the promotion of ADSCs epithelial cell differentiation by IGFBP3 (Fig. 4E).

Additionally, we assessed the effect of Igfbp3 expression on ADSC proliferation and migration in the induction medium. CCK- 8 and EDU staining results showed that Igfbp3 silencing reduced ADSC viability and proliferative capacity, while Igfbp3 overexpression enhanced these, with levels nearing those of HaCaT cells (Fig. 4F-G). Transwell and scratch assays demonstrated that Igfbp3 silencing inhibited ADSC migration ability, whereas Igfbp3 overexpression enhanced it, with migration ability similar to that of HaCaT cells (Fig. 4H-I).

These research findings indicate that ADSC cells possess the capability to differentiate into epithelial cells, and IGFBP3 can promote ADSC epithelial cell differentiation and enhance cell proliferation and migration.

IGFBP3 promotes ADSCs epithelial cell differentiation via ITGB1/ERK signaling pathway

The regulation of cell growth, survival, and migration is governed by soluble growth factors and interactions with the extracellular matrix, with integrins playing a crucial role as heterodimeric transmembrane receptors that bridge the extracellular matrix and intracellular signaling networks (Berman et al. 2003). Our previous studies have confirmed that IGFBP3 interacts with ITGB1 to activate cellular signaling (Wang et al. 2020). Studies have also reported that ITGB1 can activate the ERK signaling pathway to enhance ADSCs proliferation and epithelial differentiation, thereby facilitating wound healing (Wu et al. 2022; Chen et al. 2020).

To further investigate whether IGFBP3 promotes ADSCs epithelial differentiation via the ITGB1-mediated ERK signaling pathway, the expression of relevant proteins and their encoding genes in ADSCs cells was investigated through RT-qPCR and WB analysis. The outcomes indicate that upregulation of IGFBP3 in ADSCs cells can enhance the expression of ITGB1 and p-ERK1/2 proteins and their encoding genes, while inhibition of IGFBP3 expression downregulates the expression of ITGB1 and p-ERK1/2 proteins and their encoding genes (Fig. 5A-B). These

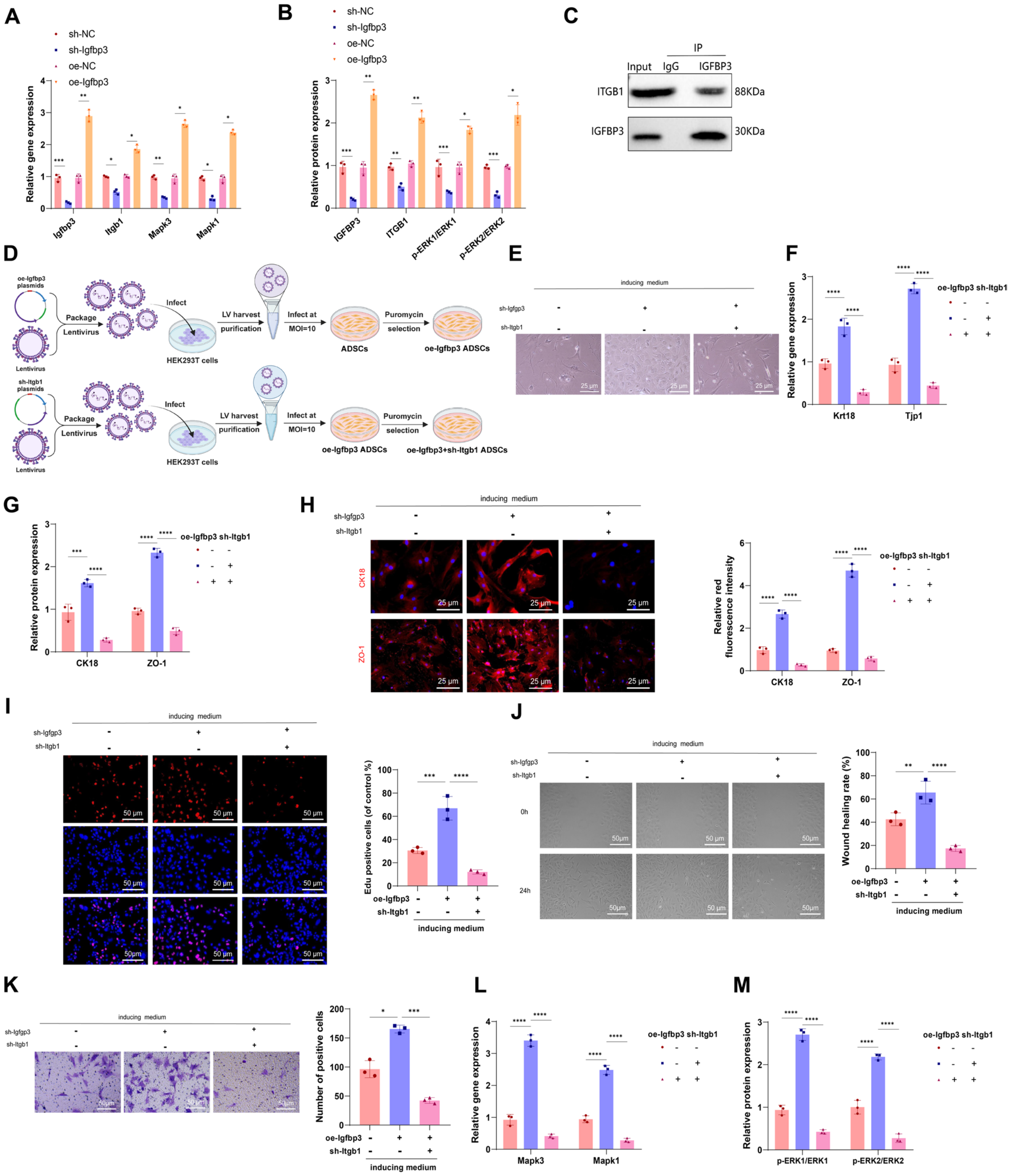

findings suggest that upregulating IGFBP3 expression in ADSCs cells activates the ITGB1/ERK signaling pathway. Furthermore, Co-IP experiments further demonstrate the connection amid IGFBP3 and ITGB1 proteins (Fig. 5C).

To substantiate IGFBP3's function in facilitating ADSCs epithelial cell differentiation through integrin ITGB1, we conducted lentivirus transfection on ADSCs cells overexpressing Igfbp3 to silence the Itgb1 gene, resulting in the generation of Itgb1

◂**Fig. 5** The influence of IGFBP3 via the ITGB1/ERK signaling pathway on ADSCs epithelial cell differentiation. Note: (**A**) RT-qPCR was conducted to assess the changes in the expression of Igfbp3, Itgb1, Mapk3, and Mapk1 mRNA in ADSCs cells after silencing or overexpressing Igfbp3; (**B**) WB analysis was performed to detect the changes in the protein expression of IGFBP3, ITGB1, ERK1, ERK2, p-ERK1, and p-ERK2 in ADSCs cells after silencing or overexpressing Igfbp3; (**C**) Co-IP experiment was conducted to investigate the interaction between IGFBP3 and ITGB1 proteins; (**D**) Schematic representation of the experiment silencing Itgb1 on the basis of overexpressing Igfbp3; (**E**) Inverted microscopy was used to observe the effects of Itgb1 silencing on the morphology of ADSCs cells (scale bar =25 μm); (**F**) RT-qPCR was performed to assess the changes in Krt18 and Tjp1 mRNA expression in ADSCs cells among different intervention groups; (**G**) WB analysis was carried out to determine the expression changes of CK18 and ZO- 1 proteins in ADSCs cells among different intervention groups; (**H**) Immunofluorescence staining was used to detect the expression changes of CK18 and ZO- 1 proteins in ADSCs cells among different intervention groups (scale bar =25 μm); (**I**) EDU experiment was conducted to evaluate the proliferation ability of ADSCs cells, where EDU-positive cells are shown in red, indicating cells in the proliferative phase, while blue represents DAPI-stained cell nuclei (scale bar =50 μm); (**J**) Scratch assay was performed to assess the migration of ADSCs cells (scale bar =50 μm); (**K**) Transwell experiment was carried out to evaluate the migration ability of ADSCs cells (scale bar =50 μm); (**L**) RT-qPCR was conducted to determine the expression changes of Mapk3 and Mapk1 mRNA; (**M**) WB analysis was performed to detect the changes in the protein expression of ERK1, ERK2, p-ERK1, and p-ERK2. Quantitative data in the figures are presented as Mean ± SD, and each experiment was repeated three times per group. Statistical significance is denoted as * for $P < 0.05$, ** for $P < 0.01$, *** for $P < 0.001$, and **** for $P < 0.0001$ when comparing between groups

gene-silenced ADSCs cells (Fig. 5D). The efficiency of Igfbp3 silencing was confirmed via RT-qPCR and WB analysis, with the cell population demonstrating the highest effectiveness being picked for further trials (Fig. S5E-F). Observation under an inverted microscope revealed that silencing Itgb1 on the foundation of Igfbp3 overexpression inhibited ADSCs epithelial cell differentiation (Fig. 5E). RT-qPCR and WB analysis demonstrated that silencing Itgb1 reversed the upregulation effect of Igfbp3 overexpression on CK18 and ZO- 1 protein expression and their encoding genes in ADSCs cells (Fig. 5F-G). Immunofluorescence staining for CK18 and ZO- 1 proteins further confirmed that silencing Itgb1 inhibited ADSCs epithelial cell differentiation (Fig. 5H). Additionally, the promotion of ADSCs cell proliferation facilitated by Igfbp3 overexpression was nullified by the repression of Itgb1, as demonstrated by the EDU staining outcomes (Fig. 5I). Transwell and scratch assays indicated that downregulation of Itgb1 counteracted the migratory stimulation caused by overexpression of Igfbp3 in ADSCs cells (Fig. 5J-K). Additionally, RT-qPCR and WB findings revealed that silencing Itgb1 on the basis of Igfbp3 overexpression inhibited the phosphorylation activation level of p-ERK1/2 proteins in ADSCs cells (Fig. 5L-M).

The above research results suggest that epithelial cell differentiation, proliferation, and migratory activities of ADSCs are augmented through the ITGB1/ERK signaling pathway activation mediated by IGFBP3.

Preparation and performance study of ADSCs-IGFBP3 peptide self-assembling hydrogel scaffold

To further validate the promoting effect of IGFBP3 protein in ADSCs cells on the repair of STI, we developed a composite hydrogel scaffold using poly(ε-caprolactone) (PCL) and gelatin (Gel) and loaded IGFBP3 protein from ADSCs cells onto this hydrogel scaffold (Fig. 6A). The results from TEM and SEM revealed that the composite materials GP and IGP exhibited smooth and uniform electrospun structures, with preliminary confirmation of IGFBP3 protein loading on the surface of IGP material (Fig. 6B).

Fourier transform infrared spectroscopy (FTIR) analysis demonstrated that there were no wavelength differences between PCL, GP, and IGP gels, but the absorption peaks of GP and IGP gels were stronger than those of PCL, indicating that GP and IGP gels possess more active functional groups. Moreover, compared to GP gel, IGP gel showed a significant increase in functional groups, suggesting successful preparation of the PCL and Gel composite gel—GP—and loading of IGFBP3 protein into the GP composite gel (Fig. 6C). Results from XRD experiments exhibited a noticeable peak at $2\theta = 21.5°$ for PCL, which decreased upon the addition of gelatin into the composite gel scaffold, indicating that gelatin can reduce the crystallinity of the material surface (Fig. 6D).

The degradation experiment results demonstrate an accelerated degradation rate of the composite gel with the addition of gelatin (Fig. 6E). Water contact angle testing reveals a decrease in the gel water contact angle with the inclusion of gelatin, indicating an enhancement in the surface hydrophilicity of the electrospun membrane compared to pure PCL (Rodríguez-Hermida et al. 2016). Previous literature suggests that contact angles between 45° and 60° are conducive to cell adhesion and growth (Fig. 6F). Moreover, upon the addition of gelatin, both the compressive modulus and swelling ratio of the composite gel significantly increase (Fig. 6G-H). The loading of IGFBP3 protein shows no significant impact on the degradation rate, water contact angle, compressive modulus, and swelling ratio of the gel.

Following the feasibility assessment of the bioink for 3D printing, we conducted 3D bioprinting experiments with cell integration (Fig. 6I-J). Inverted microscopy observations and immunofluorescence staining of the cell cytoskeleton revealed that ADSCs cells could evenly distribute in both composite gels, displaying robust viability. After the same incubation period, ADSC cells were relatively more abundant in the IGPA composite gel than in the GPA gel scaffold (Fig. 7A-B). Live/dead cell staining further confirmed the favorable survival status of ADSCs cells in both composite gel scaffolds (Fig. 7C).

In assessing the effects of IGFBP3 on the proliferation and migration of ADSCs cells, we assessed cell viability through a CCK- 8 experiment, which indicated enhanced cell activity in IGPA compared to GPA (Fig. 7D). SEM observations showed ADSCs cells adhered to and intertwined with the scaffolds; on the third and fifth days, cells displayed elongated cytoskeletal structures and spindle-shaped or polygonal morphologies, progressing to complete surface diffusion by the seventh day, forming cell membrane structures on both scaffolds, indicating good cellular compatibility. Significantly enhanced proliferation rates of ADSCs cells in the IGPA 3D printed structures were observed compared to GPA (Fig. 7E). After 24 h of culture in Transwell plates, with cells migrating to the surface under the membrane, crystal violet staining revealed that the inclusion of the IGFBP3 protein significantly improved cell mobility (Fig. 7F). Additionally, EDU staining results indicated that IGFBP3 protein enhanced the proliferative capability of ADSCs cells (Fig. 7G).

To evaluate the influence of IGFBP3 protein on ADSCs epithelial cell differentiation, we cultured the prepared 3D printed structures in an induction medium for epithelial differentiation and then assessed the expression of relevant mRNA and proteins through RT-qPCR and WB analysis. The examination findings demonstrated that relative to GPA, the inclusion of IGFBP3 protein resulted in substantially elevated expression of IGFBP3, ITGB1, CK18, and ZO- 1 proteins, as well as their encoding mRNAs in ADSCs cells within the IGPA 3D printed structures, confirming the promoting effect of IGFBP3 protein on ADSCs epithelial cell differentiation (Fig. 7H-I).

These findings indicate the successful construction of an ADSCs-IGFBP3 peptide self-assembling hydrogel scaffold. Compared to traditional PCL, the composite scaffold exhibits enhanced surface properties, swelling capacity, and in vitro biodegradation rate. Additionally, ADSC cells could effectively adhere to and survive on this scaffold.

Improvement of STI by ADSCs-IGFBP3 peptide self-assembling hydrogel scaffold via ITGB1/ERK signaling pathway

To investigate the therapeutic effects of the ADSCs-IGFBP3 peptide self-assembling hydrogel scaffold on STI repair further, we utilized the prepared hydrogel in a mouse model of STI (Fig. 8A). Through a 2-week observation period, we observed an enhancement in epidermal healing in mice treated with GPA and IGPA hydrogels as opposed to the GP group. Moreover, the IGPA group illustrated a further improvement in epidermal healing contrasted with the GPA group (Fig. 8B). H&E staining revealed that after 14 days of treatment, the GP and GPA groups showed incomplete epidermal healing at the wound edges with the presence of epithelial pseudo-tumors. In contrast, the IGPA group displayed significantly enhanced wound re-epithelialization, characterized by well-healed, uniform, and mature newly formed epidermis, orderly arranged collagen fibers in the neodermis, and a lack of pseudo-tumor-like epithelium (Fig. 8C). Masson's trichrome staining revealed a remarkable upsurge in collagen protein expression in the mouse soft tissues following treatment with GPA and IGPA hydrogels contrasted against the GP group. Furthermore, in relation to the GPA group, IGPA treatment led to further upregulation of collagen protein expression (Fig. 8D). Observations derived from the TUNEL examination revealed a substantial drop in cell apoptosis in mouse soft tissues following treatment with the IGPA hydrogel scaffold (Fig. 8E).

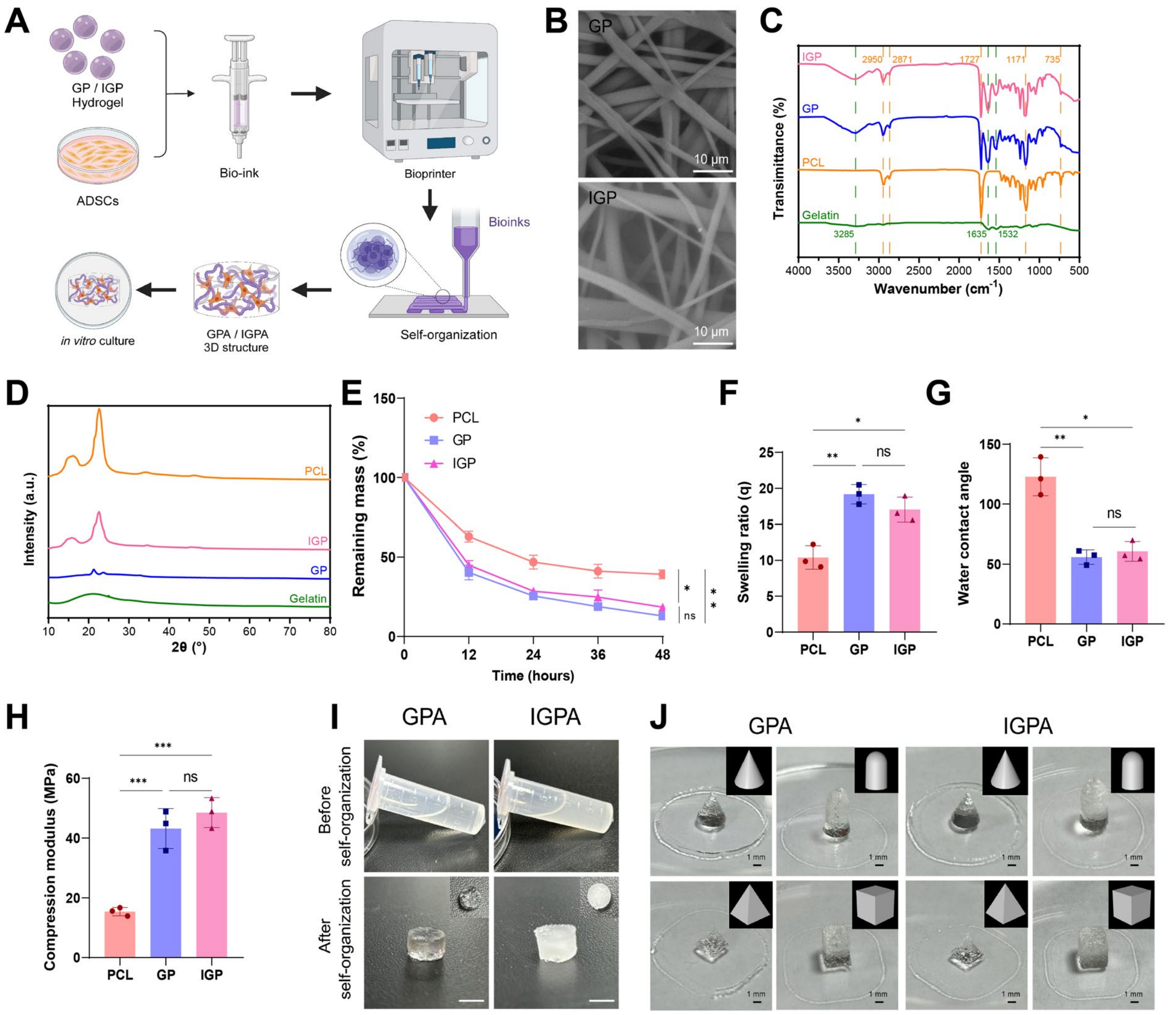

Fig. 6 Preparation and characterization of 3D bioprinting ink. Note: (**A**) Schematic diagram of the preparation process for ADSCs-IGFBP3 peptide self-assembling hydrogel scaffold; (**B**) GP and IGP composite material high-resolution scanning electron microscope image (SEM) (scale bar = 10 μm); (**C**) Characterization of gels in various groups by Fourier-transform infrared spectroscopy; (**D**) XRD spectra of gels in various groups; (**E**) Degradation curves of gels in various groups; (**F**) Water contact angle test results of each gel group; (**G**) Compressive modulus of gels in various groups; (**H**) Swelling ratio of gels in various groups; (**I**) Overall appearance of GPA and IGPA composite gels before and after self-assembly (scale bar = 1 mm); (**J**) 3D printing of cubes, cylinders, cones, and tetrahedral hydrogels made of GPA and IGPA composites, each consisting of 50 layers with a thickness of 100 μm per layer and a total height of 5 mm. The line spacing in the X–Y plane is 300 μm (scale bar = 1 mm). The quantitative data in the figures are presented as Mean ± SD, and each experiment was repeated three times. * indicates statistical significance between groups, with $^*P < 0.05$, $^{**}P < 0.01$, $^{***}P < 0.001$, and"ns"indicating no significant statistical difference

Moreover, immunohistochemistry and immunofluorescence staining analyses of the wound soft tissues revealed that the IGPA group demonstrated a considerable rise in the expression of PCNA and Ki67 proteins relative to the GP and GPA groups, indicating enhanced cell proliferation capacity in the IGPA-treated group (Fig. 8F-G). Subsequent CD34 and α-SMA immunofluorescence co-staining confirmed a significant increase in capillary density in the wound area following IGPA treatment (Fig. 8H). The discoveries suggest that IGPA facilitates cell

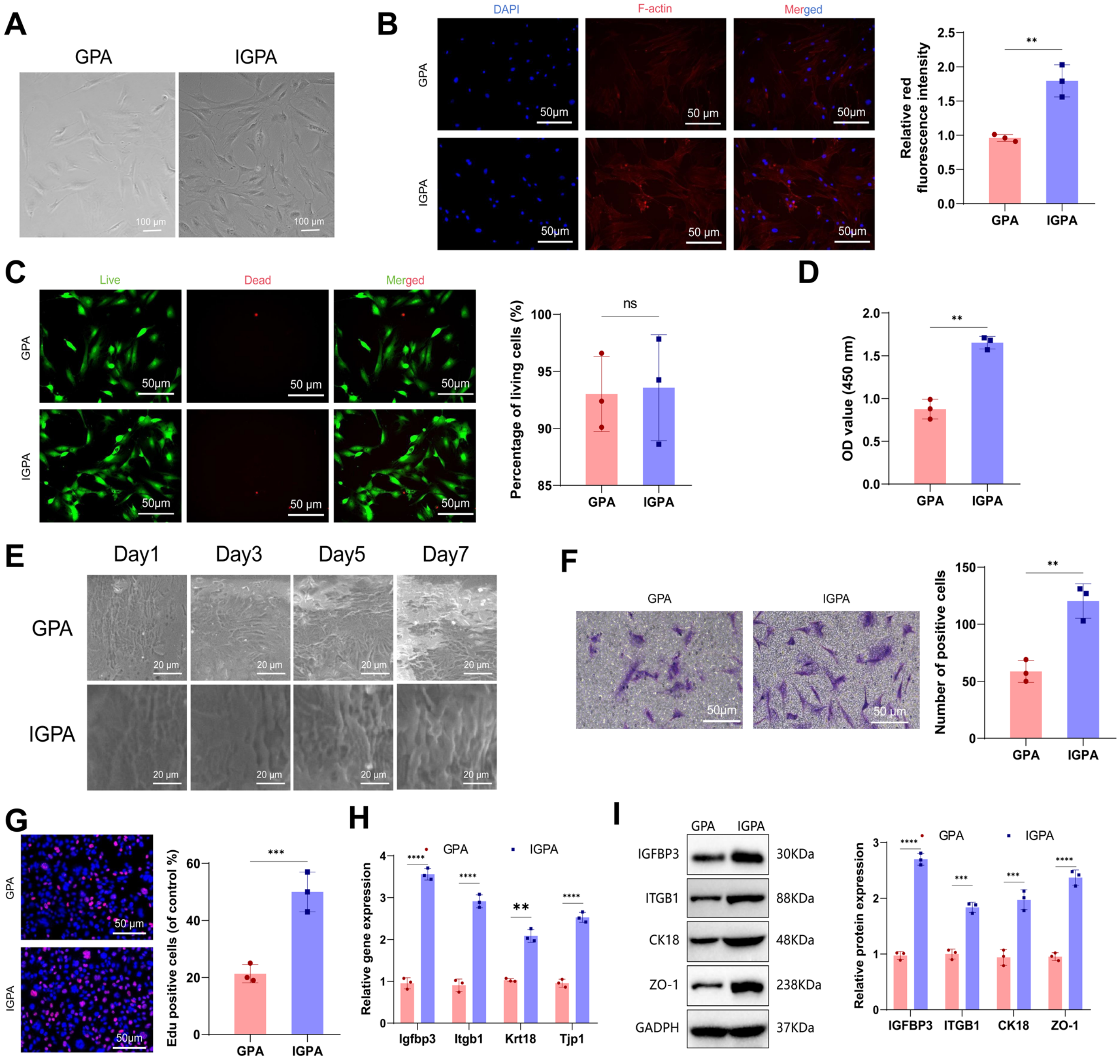

Fig. 7 Biocompatibility evaluation of 3D bioprinting scaffold materials. Note: (**A**) Morphological observation of ADSCs in the composite hydrogel scaffold using inverted microscopy (scale bar = 100 μm); (**B**) Observation of ADSCs cell skeleton in the 3D printed structure using immunofluorescence staining (scale bar = 50 μm); (**C**) Live/dead cell staining in the 3D printed structure, with green fluorescence indicating live cells and red fluorescence indicating dead cells (scale bar = 50 μm); (**D**) Assessment of ADSCs cell viability in the 3D printed structure using the CCK- 8 assay; (**E**) SEM images of ADSCs cells cultured in the hydrogel scaffold for 1, 3, 5, and 7 days (scale bar = 20 μm); (**F**) Transwell assay to evaluate the migration ability of ADSCs cells on the composite gel (scale bar = 50 μm); (**G**) EDU staining to detect the proliferation ability of ADSCs cells on the composite gel; (**H**) RT-qPCR analysis to determine the expression levels of Igfbp3, Itgb1, Krt18, and Tjp1 mRNA in ADSCs cells after epithelial differentiation induction; (**I**) WB analysis to assess the expression levels of IGFBP3, ITGB1, CK18, and ZO- 1 proteins in ADSCs cells after epithelial differentiation induction. Quantitative data in the figures are presented as Mean ± SD, and each experiment was repeated three times. * denotes statistical significance between groups, with $**P < 0.01$, $***P < 0.001$, $****P < 0.0001$, and"ns"indicating no statistically significant difference

proliferation and neovascularization in mouse soft tissues, key processes in wound healing.

Furthermore, immunohistochemistry results illustrated a noteworthy upregulation in the expression of IGFBP3, ITGB1, CK18, and ZO- 1 proteins in the soft tissue cells of mice following IGPA treatment (Fig. 8I). RT-qPCR and WB analyses further validated these results and indicated a significant upregulation in p-ERK1/2 protein expression after IGPA treatment (Fig. 8J-K).

In conclusion, our study demonstrates that the ADSCs-IGFBP3 peptide self-assembling hydrogel scaffold improves STI through the ITGB1/ERK signaling pathway.

Discussion

Prior investigations have validated the potential function of ADSCs in the repair of STI. However, this research meticulously explores the essential functionalities of ADSCs in the process of STI repair through the advanced application of single-cell multi-omics technology and 3D bioprinting models. In comparison to prior studies, this research focuses on analyzing the changes in the number of ADSCs in STI, alterations in intercellular communication, and their impact on epithelial cell differentiation, providing a more comprehensive perspective for understanding the treatment of STI (Su et al. 2021; Tang et al. 2022; Anderson et al. 2022).

IGFBP3 plays a critical role in STI repair by regulating ADSCs'epithelial cell differentiation, proliferation, and migration capabilities, thereby promoting the healing process of STI. Differing from previous studies, this research extensively examines the expression characteristics of IGFBP3 in ADSCs and the molecular mechanisms regulating cell functions, offering new clues for further exploration of mechanisms underlying STI repair (Teufelsbauer et al. 2019; Wang et al. 2019).

This study maximizes the utilization of single-cell multi-omics technology and 3D bioprinting models to deeply analyze the cellular changes during the process of STI, unveiling the characteristics of different cell subgroups and their interactions. Compared to conventional methods, this integrated approach provides a more comprehensive and three-dimensional research perspective, bringing new insights into the understanding of STI repair mechanisms.

The study primarily investigates the molecular mechanisms of IGFBP3 in regulating ADSCs'epithelial cell differentiation, revealing that IGFBP3, by upregulating the expression of ITGB1, activates the ERK signaling pathway, thereby enhancing ADSCs'epithelial cell differentiation, proliferation, and migration capabilities. This further elucidates the critical regulatory role of IGFBP3 in STI repair, offering essential clues for developing therapeutic strategies targeting relevant pathways.

The ADSCs-IGFBP3 peptide self-assembling hydrogel scaffold, as a novel therapeutic strategy, demonstrated promising efficacy in animal models in this study. This scaffold not only serves as a carrier and supporting structure for ADSCs cells but also releases IGFBP3 protein to enhance the healing process of STI (Tian et al. 2022; Wang et al. 2022). Animal model experiments revealed that the application of ADSCs-IGFBP3 peptide self-assembling hydrogel scaffold accelerated tissue repair in the injury area, reduced scar formation, and exhibited good biocompatibility and degradability. These findings provide a solid experimental basis for translating this technology into clinical applications (Liu et al. 2022; Wang 2023).

By integrating multiomics analysis with in vitro cell experiments, we successfully developed an IGPA and utilized this scaffold for the treatment of STI in mice through 3D bioprinting. Combining in vivo and in vitro experiments with 3D printing technology, preliminary conclusions were drawn: in the repair of STI, the high expression of IGFBP3 in ADSCs can promote epithelial cell differentiation, proliferation, and migration through the initiation of the ITGB1/ERK signaling pathway. The regulatory function of IGFBP3 expression in the epithelial cell differentiation process of ADSCs and its underlying molecular mechanisms for enhancing the recovery of STI are elucidated by our research, providing an essential reference for the treatment of such injuries.

This study has made significant progress in exploring the molecular mechanisms of IGFBP3 protein in ADSCs in the repair of STIs. By integrating single-cell multiomics technology and 3D bioprinting models, we have elucidated in detail the pivotal function of IGFBP3 in promoting ADSCs'epithelial cell differentiation, proliferation, and migration. This

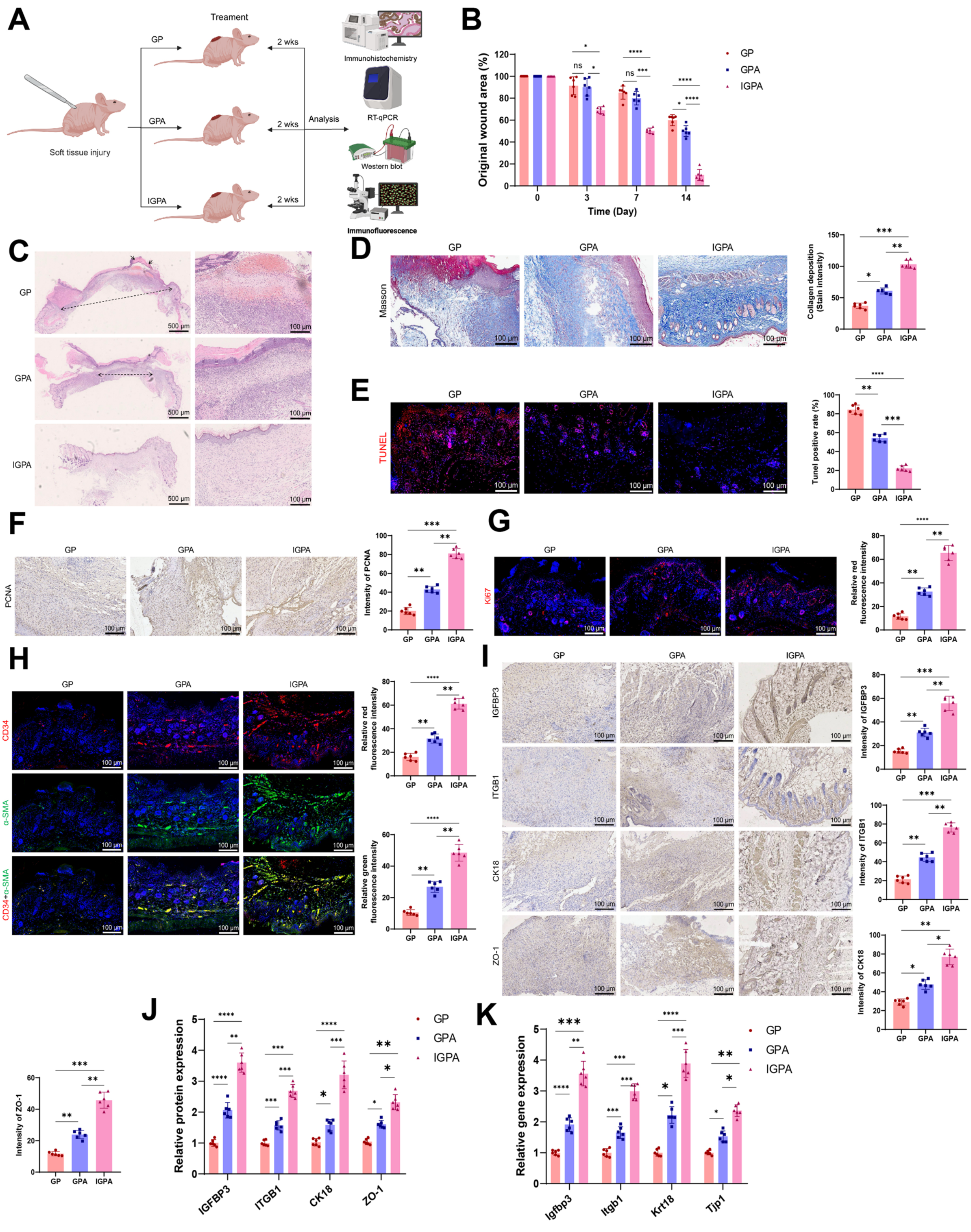
A
Soft tissue injury
Treament
GP
GPA
IGPA
2 wks
Analysis
Immunohistochemistry
RT-qPCR
Western blot
Immunofluorescence
B
Original wound area (%)
Time (Day)
0
3
7
14
ns
GP
GPA
IGPA
C
500 μm
100 μm
D
Masson
Collagen deposition (Stain intensity)
E
TUNEL
Tunel positive rate (%)
F
PCNA
Intensity of PCNA
G
Ki67
Relative red fluorescence intensity
H
CD34
α-SMA
CD34+α-SMA
Relative red fluorescence intensity
Relative green fluorescence intensity
I
IGFBP3
ITGB1
CK18
ZO-1
Intensity of IGFBP3
Intensity of ITGB1
Intensity of CK18
Intensity of ZO-1
J
Relative protein expression
IGFBP3
ITGB1
CK18
ZO-1
K
Relative gene expression
Igfbp3
Itgb1
Krt18
Tjp1

◂**Fig. 8** IGPA peptide hydrogel scaffold improves STI through the ITGB1/ERK signaling pathway. Note: (**A**) Schematic illustration of the animal experimental procedure, with 6 mice per group; (**B**) Therapeutic effects of various gel scaffolds on epidermal healing in mice; (**C**) Histological staining of mouse soft tissue with H&E, where single-headed arrows indicate non-epithelialized areas and double-headed arrows indicate the edge of granules (scale bar = 500/100 μm); (**D**) Results of Masson's staining in mouse soft tissue, showing interstitial collagen proteins in bluish-green; (**E**) TUNEL staining results of mouse soft tissue (scale bar = 100 μm); (**F**) Immunohistochemical staining depicting the expression changes of PCNA protein in mouse soft tissue among different experimental groups (scale bar = 100 μm); (**G**) Immunofluorescence staining displaying the expression changes of Ki67 protein in mouse soft tissue among different experimental groups (scale bar = 100 μm); (**H**) Immunofluorescence staining revealing the expression changes of CD34 and α-SMA proteins in mouse soft tissue among different experimental groups (scale bar = 100 μm); (**I**) Immunohistochemical staining showing the expression changes of IGFBP3, ITGB1, CK18, and ZO- 1 proteins in mouse soft tissue among different experimental groups (scale bar = 100 μm); (**J**) WB analysis of IGFBP3, ITGB1, ERK1, ERK2, p-ERK1, and p-ERK2 protein expressions in mouse soft tissue; (K) RT-qPCR assessment of Igfbp3, Itgb1, Mapk3, and Mapk1 mRNA expressions in mouse soft tissue. Quantitative data in the figures are expressed as Mean ± SD, with 6 mice per group. * indicates statistical significance between groups, $*P < 0.05$, $**P < 0.01$, $***P < 0.001$, $****P < 0.0001$

breakthrough identifies innovative molecular targets that could revolutionize the treatment of STIs, demonstrating significant scientific value. In the future, further research could focus on investigating the interactions of IGFBP3 with other growth factors or signaling pathways, as well as assessing the feasibility and safety of clinical translation to expand the clinical application prospects of this research.

However, several limitations exist in this study that require attention. Firstly, the experimental results should be validated for their stability and reliability in a larger sample size. Additionally, it is important to recognize the inherent differences between animal models and the human physiological environment, necessitating further validation through comprehensive clinical data analysis. Furthermore, while this study delves into the mechanism of action of IGFBP3 in STI repair, it is essential to consider the potential impact of other regulatory factors on the healing process in order to develop a thorough comprehension of the intricacy of STI recovery.

Looking ahead, future prospects include the optimization of 3D bioprinting models to better mimic the microenvironment of STI, combined with the integration of advanced technologies such as gene editing and stem cell engineering to enhance research on the role of IGFBP3 in STI repair mechanisms. Moreover, exploring the feasibility and effectiveness of applying IGFBP3 to the treatment of STI through preclinical research and clinical trials could pave the way for more personalized and efficient treatment strategies for patients.

Author contributions Sirui Tian: Software, Resources, Investigation. Haiyang Yu: Writing – original draft, Validation, Software, Resources, Methodology, Investigation, Formal analysis. Ruoxuan Yang: Software, Resources, Investigation. Baohong Zhao: Writing – review & editing, Validation, Project administration, Methodology, Funding acquisition, Conceptualization. Heshi Wang: Writing – review & editing, Validation, Project administration, Methodology, Funding acquisition, Conceptualization. Danning Wang: Writing – review & editing, Validation, Project administration, Methodology, Funding acquisition, Conceptualization.

Funding This study was supported by Liaoning Provincial Department of Science and Technology (2022-BS- 142), National Natural Science Foundation of China (82071151).

Data availability The datasets generated and/or analysed during the current study are not publicly available but are available from the corresponding author on reasonable request.

Declarations

Ethics approval and consent to participate This study was approved by the Ethics Committee of China Medical University (Approval No. KT20240661). All procedures performed in studies involving human participants were in accordance with the ethical standards of the institutional and/or national research committee and with the 1964 Helsinki Declaration and its later amendments or comparable ethical standards. Informed consent was obtained from all individual participants included in the study. Participation was voluntary, and participants had the right to withdraw at any time without any consequences. All personal data collected during the study were kept confidential and used solely for research purposes.

Consent for publication Not applicable.

Competing interest The authors declare no competing interests.

References

Al-Ghadban S, Bunnell BA. Adipose tissue-derived stem cells: Immunomodulatory effects and therapeutic potential. Physiology (Bethesda). 2020;35(2):125–33. https://doi.org/10.1152/physiol.00021.2019.

Ali F, Khan I, Chen J, Akhtar K, Bakhsh EM, Khan SB. Emerging fabrication strategies of hydrogels and its applications. Gels. 2022;8(4):205. Published 2022 Mar 24. https://doi.org/10.3390/gels8040205

Anderson AE, Wu I, Parrillo AJ, et al. An immunologically active, adipose-derived extracellular matrix biomaterial for soft tissue reconstruction: concept to clinical trial. NPJ Regen Med. 2022;7(1):6. Published 2022 Jan 14. https://doi.org/10.1038/s41536-021-00197-1

Baka Z, Godier C, Lamy L, et al. A coculture based, 3D bioprinted ovarian tumor model combining cancer cells and cancer associated fibroblasts. Macromol Biosci. 2023;23(3):e2200434. https://doi.org/10.1002/mabi.202200434.

Berman AE, Kozlova NI, Morozevich GE. Integrins: structure and signaling. Biochemistry (Mosc). 2003;68(12):1284–99. https://doi.org/10.1023/b:biry.0000011649.03634.74.

Chang X, Zheng Y, Xu K. Single-cell RNA sequencing: technological progress and biomedical application in cancer research. Mol Biotechnol. 2024;66(7):1497–519. https://doi.org/10.1007/s12033-023-00777-0.

Chao CC, Lee WF, Yang WH, et al. IGFBP-3 stimulates human osteosarcoma cell migration by upregulating VCAM-1 expression. Life Sci. 2021;265:118758. https://doi.org/10.1016/j.lfs.2020.118758.

Chen L, Zheng Q, Liu Y, et al. Adipose-derived stem cells promote diabetic wound healing via the recruitment and differentiation of endothelial progenitor cells into endothelial cells mediated by the VEGF-PLCγ-ERK pathway. Arch Biochem Biophys. 2020;692:108531. https://doi.org/10.1016/j.abb.2020.108531.

Chen M, Jiang R, Deng N, Zhao X, Li X, Guo C. Natural polymer-based scaffolds for soft tissue repair. Front Bioeng Biotechnol. 2022;10:954699. Published 2022 Jul 19. https://doi.org/10.3389/fbioe.2022.954699

Cherief M, Negri S, Qin Q, et al. TrkA+ neurons induce pathologic regeneration after soft tissue trauma. Stem Cells Transl Med. 2022;11(11):1165–76. https://doi.org/10.1093/stcltm/szac073.

Fernández-Ponce C, Geribaldi-Doldán N, Sánchez-Gomar I, et al. The role of glycosyltransferases in colorectal cancer. Int J Mol Sci. 2021;22(11):5822. Published 2021 May 30. https://doi.org/10.3390/ijms22115822

Galbo PM Jr, Zang X, Zheng D. Molecular features of cancer-associated fibroblast subtypes and their implication on cancer pathogenesis, prognosis, and immunotherapy resistance. Clin Cancer Res. 2021;27(9):2636–47. https://doi.org/10.1158/1078-0432.CCR-20-4226.

Huang J, Yu J, Wang J, et al. Novel potential biomarkers for severe alcoholic liver disease. Front Immunol. 2022;13:1051353. Published 2022 Dec 13. https://doi.org/10.3389/fimmu.2022.1051353

Huang Q, Zou Y, Arno MC, et al. Hydrogel scaffolds for differentiation of adipose-derived stem cells. Chem Soc Rev. 2017;46(20):6255–75. https://doi.org/10.1039/c6cs00052e.

Kalisky T, Blainey P, Quake SR. Genomic analysis at the single-cell level. Annu Rev Genet. 2011;45:431–45. https://doi.org/10.1146/annurev-genet-102209-163607.

Khazaei S, Keshavarz G, Bozorgi A, Nazari H, Khazaei M. Adipose tissue-derived stem cells: a comparative review on isolation, culture, and differentiation methods [published correction appears in Cell Tissue Bank. 2021 Dec;22(4):737. https://doi.org/10.1007/s10561-021-09928-6]. Cell Tissue Bank. 2022;23(1):1–16. https://doi.org/10.1007/s10561-021-09905-z

Leale DM, Li L, Settles ML, et al. A two-stage digestion of whole murine knee joints for single-cell RNA sequencing. Osteoarthr Cartil Open. 2022;4(4):100321. Published 2022 Nov 24. https://doi.org/10.1016/j.ocarto.2022.100321

Li Q, Zhao H, Xia S, Wei H, Chen F, Jin P. RUNX2 promotes epithelial differentiation of ADSCs and burn wound healing via targeting E-cadherin. Oncotarget. 2017;9(2):2646–2659. Published 2017 Dec 21. https://doi.org/10.18632/oncotarget.23522

Li S, Yu Q, Li H, Chen M, Jin Y, Liu D. Self-assembled peptide hydrogels in regenerative medicine. Gels. 2023;9(8):653. Published 2023 Aug 14. https://doi.org/10.3390/gels9080653

Liu Y, Cheng F, Wang ZW, et al. Zhonghua Shao Shang Yu Chuang Mian Xiu Fu Za Zhi. 2024;40(1):50-56https://doi.org/10.3760/cma.j.cn501225-20230928-00101

Liu Z, Zeng S, Quan X. Image genetic analysis and application research based on QRFPR and other neural network-related SNP Loci [retracted in: Biomed Res Int. 2023 Jun 21;2023:9754165. https://doi.org/10.1155/2023/9754165]. Biomed Res Int. 2022;2022:5861928. Published 2022 Aug 16. https://doi.org/10.1155/2022/5861928

Mazini L, Rochette L, Admou B, Amal S, Malka G. Hopes and Limits of Adipose-Derived Stem Cells (ADSCs) and Mesenchymal Stem Cells (MSCs) in wound healing. Int J Mol Sci. 2020;21(4):1306. Published 2020 Feb 14. https://doi.org/10.3390/ijms21041306

Méar L, Hao X, Hikmet F, Damdimopoulou P, Rodriguez-Wallberg KA, Lindskog C. Transcriptomics and spatial proteomics for discovery and validation of missing proteins in the human ovary. J Proteome Res. 2024;23(1):238–48. https://doi.org/10.1021/acs.jproteome.3c00545.

Nabil S, Nordin R, Rashdi MF. Are facial soft tissue injury patterns associated with facial bone fractures following motorcycle-related accident? J Oral Maxillofac Surg. 2022;80(11):1784–94. https://doi.org/10.1016/j.joms.2022.07.144.

Nie P, Zhang C. Effect of vacuum sealing drainage on soft tissue injury of traumatic fracture and its effect on wound recovery. Evid Based Complement Alternat Med. 2022;2022:7107090. Published 2022 Sep 29. https://doi.org/10.1155/2022/7107090

Nynca A, Swigonska S, Molcan T, Petroff BK, Ciereszko RE. Molecular action of tamoxifen in the ovaries of rats with mammary neoplasia. Int J Mol Sci. 2023;24(21):15767. Published 2023 Oct 30. https://doi.org/10.3390/ijms242115767

Pozojevic J, Spielmann M. Single-cell sequencing in neurodegenerative disorders. Mol Diagn Ther. 2023;27(5):553–61. https://doi.org/10.1007/s40291-023-00668-9.

Ren S, Chen J, Duscher D, et al. Microvesicles from human adipose stem cells promote wound healing by optimizing cellular functions via AKT and ERK signaling pathways. Stem Cell Res Ther. 2019;10(1):47. Published 2019 Jan 31. https://doi.org/10.1186/s13287-019-1152-x

Ritchie ME, Phipson B, Wu D, et al. limma powers differential expression analyses for RNA-sequencing and microarray studies. Nucleic Acids Res. 2015;43(7):e47. https://doi.org/10.1093/nar/gkv007.

Rodríguez-Hermida S, Tsang MY, Vignatti C, et al. Switchable surface hydrophobicity-hydrophilicity of a metal-organic framework. Angew Chem Int Ed Engl. 2016;55(52):16049–53. https://doi.org/10.1002/anie.201609295.

Schneider I, Calcagni M, Buschmann J. Adipose-derived stem cells applied in skin diseases, wound healing and skin defects: a review. Cytotherapy. 2023;25(2):105–19. https://doi.org/10.1016/j.jcyt.2022.08.005.

Song S, Zhang G, Chen X, et al. HIF-1α increases the osteogenic capacity of ADSCs by coupling angiogenesis and osteogenesis via the HIF-1α/VEGF/AKT/mTOR signaling pathway. J Nanobiotechnology. 2023;21(1):257. Published 2023 Aug 7. https://doi.org/10.1186/s12951-023-02020-z

Stelzer G, Rosen N, Plaschkes I, et al. The GeneCards suite: From gene data mining to disease genome sequence analyses. Curr Protoc Bioinformatics. 2016;54:1.30.1–1.30.33. Published 2016 Jun 20. https://doi.org/10.1002/cpbi.5

Su X, Wang T, Guo S. Applications of 3D printed bone tissue engineering scaffolds in the stem cell field. Regen Ther. 2021;16:63–72. Published 2021 Feb 5. https://doi.org/10.1016/j.reth.2021.01.007

Sun LX, Wu S, Zhang XW, Liu WJ, Zhang LJ. Zhonghua Shao Shang Yu Chuang Mian Xiu Fu Za Zhi. 2022;38(7):629-639https://doi.org/10.3760/cma.j.cn501225-20220215-00029

Tang H, He Y, Liang Z, Li J, Dong Z, Liao Y. The therapeutic effect of adipose-derived stem cells on soft tissue injury after radiotherapy and their value for breast reconstruction. Stem Cell Res Ther. 2022;13(1):493. Published 2022 Oct 4. https://doi.org/10.1186/s13287-022-02952-7

Teufelsbauer M, Rath B, Moser D, Haslik W, Huk I, Hamilton G. Interaction of adipose-derived stromal cells with breast cancer cell lines. Plast Reconstr Surg. 2019;144(2):207e–17e. https://doi.org/10.1097/PRS.0000000000005839.

Thornhill JP, Barkati S, Walmsley S, et al. Monkeypox virus infection in humans across 16 countries - April-June 2022. N Engl J Med. 2022;387(8):679–91. https://doi.org/10.1056/NEJMoa2207323.

Tian A, Xue J, Sun N. Advantages of self-assembled nano peptide hydrogels in biological tissue engineering. Curr Protein Pept Sci. 2022;23(6):395–401. https://doi.org/10.2174/1389203723666220617093402.

Wang C, Li Z, Zhang K, Zhang C. Self-assembling peptides with hBMP7 biological activity promote the differentiation of ADSCs into nucleus pulposus-like cells. J Orthop Surg Res. 2022;17(1):197. Published 2022 Apr 2. https://doi.org/10.1186/s13018-022-03102-8

Wang D, Gao J, Zhao C, et al. Cyclin G2 inhibits oral squamous cell carcinoma growth and metastasis by binding to IGFBP3 and regulating the FAK-SRC-STAT signaling pathway. Front Oncol. 2020;10:560572. Published 2020 Nov 6. https://doi.org/10.3389/fonc.2020.560572

Wang L. Value of brain injury-related indicators based on neural network in the diagnosis of neonatal hypoxic-ischemic encephalopathy. Open Life Sci. 2023;18(1):20220686. Published 2023 Aug 30. https://doi.org/10.1515/biol-2022-0686

Wang T, Wang L, Zhang L, Long Y, Zhang Y, Hou Z. Single-cell RNA sequencing in orthopedic research. Bone Res. 2023;11(1):10. Published 2023 Feb 24. https://doi.org/10.1038/s41413-023-00245-0

Wang X, Wang Y, Zhou X, Liu F. Conditioned medium from adipose-derived stem cell inhibits Jurkat cell proliferation through TGF-β1 and p38/MAPK pathway. Anal Cell Pathol (Amst). 2019;2019:2107414. Published 2019 Dec 19. https://doi.org/10.1155/2019/2107414

Wu X, Guo H, Jia Y, et al. Adipose mesenchymal stem cell-based tissue engineering mesh with sustained bFGF release to enhance tissue repair. Biomater Sci. 2022;10(12):3110–3121. Published 2022 Jun 14. https://doi.org/10.1039/d1bm01893k

Xiang J, Shen J, Zhang L, Tang B. Identification and validation of senescence-related genes in circulating endothelial cells of patients with acute myocardial infarction. Front Cardiovasc Med. 2022;9:1057985. Published 2022 Dec 13. https://doi.org/10.3389/fcvm.2022.1057985

Xu X, Zhou Y, Zheng K, Li X, Li L, Xu Y. 3D polycaprolactone/gelatin-oriented electrospun scaffolds promote periodontal regeneration. ACS Appl Mater Interfaces. 2022;14(41):46145–60. https://doi.org/10.1021/acsami.2c03705.

Yi K, Li Q, Lian X, Wang Y, Tang Z. Utilizing 3D bioprinted platelet-rich fibrin-based materials to promote the regeneration of oral soft tissue. Regen Biomater. 2022;9:rbac021. Published 2022 Apr 13. https://doi.org/10.1093/rb/rbac021